Cyclohexanone-Based Chalcones as Alternatives for Fuel Additives

Lóide O. Sallum,* Vitor S. Duarte, Jean M. F. Custodio, Eduardo C. M. Faria, Aline M. da Silva, Rosa S. Lima, Ademir J. Camargo, and Hamilton B. Napolitano*
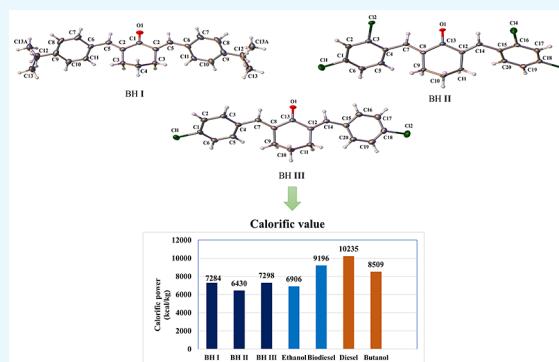
ACCESS | Metrics & More | Article Recommendations | SI Supporting Information

ABSTRACT: The use of small molecules, such as chalcones and their derivatives, for more efficient fuels is in increasing demand due to environmental factors. Here, three crystal structures (BH **I**, **II**, and **III**) of cyclohexanone-based chalcones were synthesized and described by single-crystal X-ray diffraction and Hirshfeld surface analysis. The supramolecular modeling analysis on the hyperconjugative interaction energies and QTAIM analysis at the ωB97XD/6-311++G(d,p) level of theory were carried out to analyze the intermolecular interactions in the solid-state. The structure−property relationship, frontier molecular orbital, molecular electrostatic potential, and the experimental calorific value analysis show that the three compounds are a good alternative to be used as an additive for some fuels. Our findings represent a further step forward in the development of cheaper and more efficient fuel additives and pose an opportunity for further investigation on similar analogues.

INTRODUCTION

The push from the exhaustion of fossil fuels and global warming problems has increased the demand for alternative bioenergy sources and improved the efficiency of current fuels.[1] Regarding currently used biofuels, their energetic efficacy is affected by inherent stability, oxidation, and energy availability limitations.[2] The use of small molecules for these purposes is an attractive alternative, once they usually are easily synthesized, cost-wise accessible, and serve for a myriad of different applications, including the modulation of protein−protein interactions, alteration of protein function, catalytic activity, and energy source for crucial chemical reactions.[3] In fact, due to its physicochemical properties similar to cellulose, the small molecule α-cyclodextrin has been investigated as an accurate way to unveil the chemical mechanisms involved during high-temperature conversion to biofuel.

Chalcones and their analogues are either found in plants or obtained from specific synthetic pathways and have shown numerous applications as liquid crystal materials,[4] pH sensors,[5,6] nonlinear optical materials,[7,8] as well as their remarkable biological properties: antitumor,[9,10] anti-inflammatory,[11] antifungal,[12−14] antibacterial,[12,15,16] and antioxidant.[17−20] Some of these properties can be related to fuel applications, such as energy efficiency or additives,[21−27] and often fuels such as ethanol and biofuels are prone to suffer from degradation and oxidation problems, mainly caused by micro-organisms[28−34] or even the lower combustion capacity, therefore, a lower energy efficiency.[35−39]

Chalcone molecular structures have stimulated studies of their spatial conformation systems, such as π-electronic conjugations,[40] cyclohexanone rings,[41] electronic effects of substituents in the aromatic rings,[42] interaction energies, and electronic properties obtained by density functional theory (DFT) calculations.[43] Understanding these interactions has been applied to comprehend these physical chemistry systems and pharmaceutical and material properties. X-ray crystallography, Hirshfeld surface analysis, and theoretical studies are handy tools for this subject.

Based on these potentials as fuel additives previously described for chalcones, we hypothesized that cyclohexanone-based analogues would present the same physicochemical features needed to improve biofuel's efficiency. Here we report the results of the (2E,6E)-2,6-bis(4-ethylbenzylidene)-cyclohexanone (BH **I**), (2E,6E)-2,6-bis(2,4-dichlorobenzylidene)cyclohexanone (BH **II**), and (2E,6E)-2,6-bis(4-chlorobenzylidene)cyclohexanone (BH **III**) from single-crystal X-ray diffraction (XRD) and Hirshfeld surface (HS) analysis in order to describe its molecular and supramolecular architectures. In addition to molecular structure studies, theoretical calculations such as frontier molecular orbital (FMO), molecular electrostatic potential (MEP) map, hyperconjugative interaction energies, counterpoise procedure, quantum theory of atoms in molecules (QTAIM), and
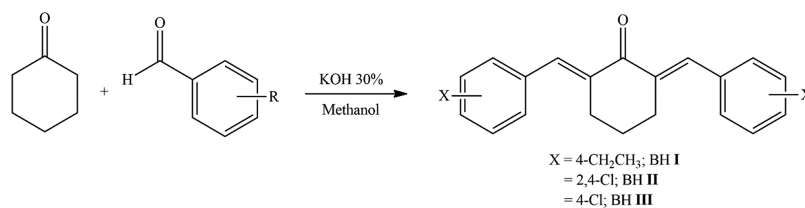
Scheme 1. Chemical Scheme of the Synthesized BH I, II, and III

X = 4-CH₂CH₃; BH **I**
= 2,4-Cl; BH **II**
= 4-Cl; BH **III**

vibrational infrared (IR) spectra assignments were carried out at the ωB97XD/6-311++G(d,p) level of theory. Finally, we quantified their energetic potential using a calorimetric pump, which was then compared to ethanol, biodiesel, diesel, and butanol.

■ EXPERIMENTAL AND COMPUTATIONAL PROCEDURES

Synthesis and Crystallization. The reaction was carried out at room temperature where BH **I**, **II**, and **III** were prepared by the reaction of cyclohexanone (3.00 mmol) and substituted benzaldehydes (2.00 mmol) in a minimum amount of absolute methanol (10 mL) as shown in Scheme 1. Then a 30% KOH solution was added and after a few minutes of continuous stirring, the reaction was completed, and the precipitate obtained was collected by filtration. Yellow product was obtained in 75% yield.

Crystals of BH **I**, **II**, and **III** were grown in dichloromethane inside a beaker with a known solvent volume. Then, the reaction mixture was kept at room temperature for slow evaporation for 96 h until the formation of crystals. All solvents and chemicals used in the synthesis were obtained from commercial sources and used without further purification. Thin-layer chromatography (TLC) was carried out using Silica gel 60 UV$_{254}$ plates, and the solvent system was ethyl acetate−hexane (3:7). Infrared (IR) spectra were recorded using a PerkinElmer-8400S FT-IR (400−4000 cm^{-1}) with the KBr pellet technique. ^{1}H and ^{13}C nuclear magnetic resonance (NMR) spectra were recorded on a Bruker 500 MHz NMR spectrometer using CDCl$_3$ as solvent. IR, ^{1}H, and ^{13}C NMR data of the representative BH **I**, **II**, and **III** are given as follows:

BH I. C$_{24}$H$_{26}$O (330.462 g/mol); yellow solid, 75% yield. IR (KBr) (cm^{-1}): 3084, 3048, 3023, 3001, 2965, 2929, 2853, 1663, 1606, 1580, 1508, 1457, 1165, 1140, 828; ^{1}H NMR (500 MHz, CDCl$_3$): δ 1.28 (6H, t, *J* = 7.5), 1.82 (2H, dtt, *J* = 14.2, 6.5, 2.8 Hz), 2.70 (4H, ddd, *J* = 14.6, 6.5, 2.8 Hz), 2.96 (4H, q, *J* = 7.5), 7.27 (4H, d, *J* = 7.99; 1.43; 0.46), 7.48 (4H, d, *J* = 8.1, 1.4, 0.5 Hz), 7.82 (2H, s), as shown in Figure S1. ^{13}C NMR (125 MHz, CDCl$_3$ δ (ppm): 190.19 (C-13), 136.71 (C-7/14), 135.85(C-8/12), 145.11 (C-1/18), 133.45 (C-4/15), 127.87 (C-3/5/16/20), 130.67 (C-2/6/17/19), 28.83 (C-21/23), 28.55 (C-9/11), 23.10 (C-10), 15.41 (C-22/24), as shown in Figure S4.

BH II. C$_{20}$H$_{14}$Cl$_4$O (412.136 g/mol); yellow solid, 75% yield. IR (KBr) (cm^{-1}): 3095, 3030, 2972, 2943, 2845, 1600, 1580, 1468, 1139, 1049, 825, 742; ^{1}H NMR (500 MHz, CDCl$_3$): δ 1.80 (2H, dtt, *J* = 14.5; 6.54; 2.75), 2.76 (4H, ddd, *J* = 14.65; 6.5, 2.8 Hz), 7.28 (4H, dd, *J* = 8.28), 7.48 (2H, d, *J* = 8.28; 1.74 Hz), 7.84 (2H, s), as shown in Figure S2. ^{13}C NMR (125 MHz, CDCl$_3$ δ (ppm): 189.54 (C-13), 138.04 (C-7/14), 135.82 (C-8/12), 133.03 (C-1/18), 132.07 (C-4/15), 134.92 (C-3/16), 131.11 (C-5/20), 128.7−129.68 (C-2/6/17/19), 28.24 (C-9/11), 23.05 (C-10), as shown in Figure S5.

BH III. C$_{20}$H$_{16}$Cl$_2$O (343.24 g/mol); yellow solid, 75% yield. IR (KBr) (cm^{-1}): 3088, 3059, 3030, 2929, 2871, 2835, 1667, 1606, 1577, 1486, 1147, 1092, 836, 799; ^{1}H NMR (500 MHz, CDCl$_3$): δ 1.81 (2H, dtt, *J* = 14.2, 6.5, 2.8 Hz), 2.36 and 2.91 (4H, ddd, *J* = 14.6, 6.5, 2.8 Hz), 7.45−7.59 (10H, 7.72 (s), 7.32 (ddd, *J* = 8.1, 1.4, 0.5 Hz), 7.40 (ddd, *J* = 8.1, 1.4, 0.5 Hz), as shown in Figure S3. ^{13}C NMR (125 MHz, CDCl$_3$ δ (ppm): 189.75 (C-13), 136.49 (C-7/14), 135.8 (C-8/12), 134.55 (C-1/18), 131.75 (C-4/15), 130.89 (C-3/5/16/20), 128.30 (C-2/6/17/19), 28.03 (C-9/11), 23.07 (C-10), as shown in Figure S6.

Crystallographic Characterization. Single-crystal XRD intensity data collection was performed on a Bruker APEX II CCD diffractometer fitted with MoKα radiation (0.71073 Å) at 120 K. The structures, using the ShelXS[44] structure solution program, were solved by direct methods and refined by least-squares minimization using the ShelXL[45] refinement package. The non-hydrogen atoms were refined anisotropically. The hydrogen atoms were placed geometrically and refined using a riding model with their Uiso set to 1.2 Ueq of the bonded carbon, except for the CH$_3$, whose Uiso(H) was set to 1.5 Ueq of the corresponding carbon. The crystallographic information file (CIF) was prepared using Olex2.[46] Also, the artwork representations for publication were prepared using the programs Ortep[47] and Mercury (version 3.0).[48] Intermolecular interactions were checked by the Platon software.[49] The BH **I**, **II**, and **III** structures were deposited in the Cambridge Structural Database under codes 2120122, 2120123, and 2120124. These data can be obtained free of charge via http://www.ccdc.cam.ac.uk/conts/retrieving.html.

Hirshfeld Surface. The HS consists of a spatial map to visualize the surface of the molecules.[50] It is a useful tool that compares the electron density of a molecule to the entire crystal and measures the distribution of close contact interactions. A weight function $w_a(\mathbf{r})$ for a molecule in a crystal was defined by eq 1,

$$w_a(r) = \sum_{a \in molecule} \rho_a(r) \Big/ \sum_{a \in crystal} \rho_a(r) \tag{1}$$

where $\rho_a(r)$ is the electron density function of the atom, centered on the nucleus a, defined by eq 2,

$$\rho_a(r) = w_a(r)\rho^{mol}(r) \tag{2}$$

$\rho^{mol}(r)$ defines the molecular electron density. In an HS, d_e is the distance from the nearest nucleus to a molecule outside the surface, which provides the close intermolecular contacts, while d_i is the distance from inside to the surface, which provides studies of the molecule itself. The normalized contact distance (d_{norm}), which combines the normalized d_e and d_i with the van der Waals radius for each atom involved in this close contact to the surface, is given by eq 3 and was used to analyze intermolecular interactions.

$$d_{norm} = (d_i - r_i^{vdw})/r_i^{vdw} + (d_e - r_e^{vdw})/r_e^{vdw} \tag{3}$$

Table 1. Vibrational Assignments of the Theoretical and Experimental FT-IR for BH I, II, and III[a]

vibrational modes	BH I		BH II		BH III	
	exptl freq[b]	scaled freq[b,c]	exptl freq[b]	scaled freq[b,c]	exptl freq[b]	scaled freq[b,c]
ν (C_{sp}^2–H) $_{Ar}$[d]$_{,Alk}$[e]	3084–3001	3044–3001	3095–3030	3042–3000	3088–3030	3044–3000
ν (C_{sp}^3–H)	2965–2853	2957–2876	2972–2845	2935–2859	2929–2835	2932–2849
ν (C=C) $_{Ar}$[d]	1606, 1580, 1508, 1457	1607, 1482	1600, 1580, 1468	1620, 1575, 1440	1606, 1577, 1486	1617, 1591, 1457
ν (C=O) and ν (C=C) $_{Alk}$[e]	1663	1683	1660	1688	1667	1682
δ (C–H) $_{Alk}$[e] out of plane	828	822	825	817	836	815
ν (C–Cl)			742	746	799	785

[a]These results were obtained at the ωB97XD/6-311++G(d,p) level of theory in the gas phase. ν = stretching; δ = bending. [b]cm^{-1}. [c]Scale factor 0.9461. [d]Ar = aromatic ring. [e]Alk = alkene.

In eq 3, the r_i^{vdw} and r_e^{vdw} represent the van der Waals radii.

The shape index is a function of a surface that allows one to identify complementarity between molecules in the crystal packing structure and that can identify hydrophobic intermolecular interactions.[51] Fingerprint plots provide a quantitative value for the types of intermolecular contacts, also known as frequency occurrences. The software Crystal Explorer 21.5[52] was used to generate HS intermolecular interactions and calculated 2D fingerprint plots.

CALORIFIC POWER

The calorific value of fuel indicates energy released by combustion per unit mass. The test to determine the calorific value was carried out in a calorimetric pump with a combustor surrounded by water. This analysis followed the ASTM D4809 standard[53] methodologies using an IKA C200 equipment. The combustor is pressurized (30 bar), and the sample is heated by an electric current that promotes burning. Burning releases energy into the environment and exchanges heat with water, generating a change in its temperature. A high precision resistive sensor measures the change in temperature as a function of time and, after correlation with the sample mass obtained prior to burning, the result of the calorific value of the sample is reported.[24,54]

Theoretical Calculation. The electronic structure calculations were carried out with the Gaussian 16[55] program package for BH I, II, and III. Full geometry optimization was carried out using DFT, with exchange-correlation functional ωB97XD[56] and basis set 6-311++G(d,p). This functional includes empirical dispersion with long-range corrections, making it suitable for noncovalent interactions. The wave function for the natural bond orbital (NBO) analysis was carried out at the same level of theory, and the basis set superposition errors (BSSE) were corrected using the counterpoise procedure as implemented in the g16 program.[57] Also, the studied electronic properties: the highest occupied molecular orbital (HOMO), the lowest unoccupied molecular orbital (LUMO) and MEP were calculated. The QTAIM analysis, using the Multwfn program (version 3.7),[58] was performed using the non-hydrogen atoms taken from the crystallographic data, while the hydrogen atoms were optimized using the same level of theory and were also calculated assignments of infrared vibrational frequencies.

RESULTS AND DISCUSSION

Solid-State Description. Table 1 lists the main IR absorption bands and also Figure 1 shows the overlapping of the theoretical and experimental FT-IR spectra for BH I, II, and III. The values of DFT in vibrational frequencies for the results obtained at the ωB97XD/6-311++G(d,p) level of theory were
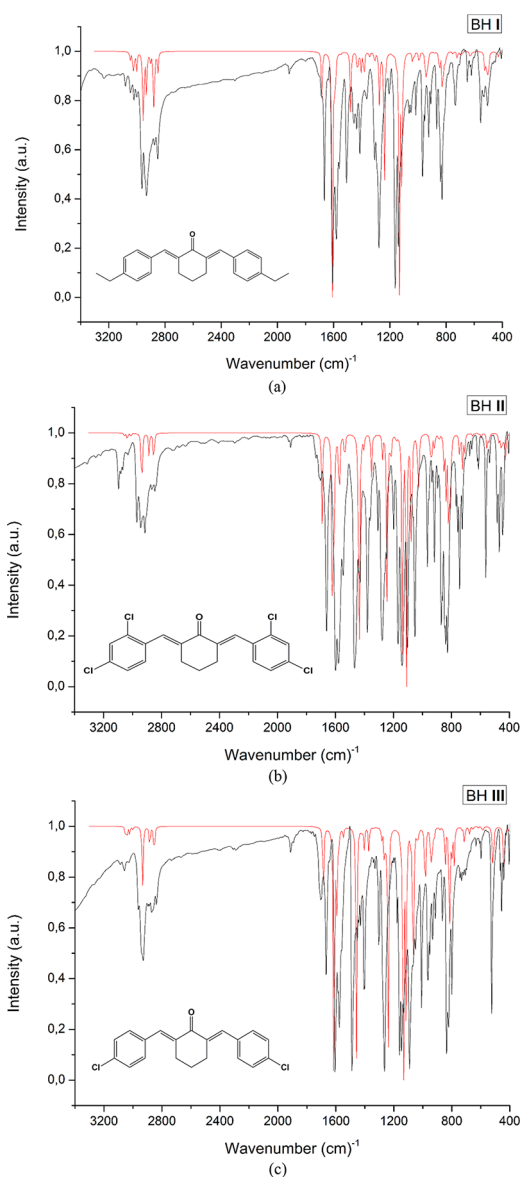

Figure 1. Overlapping of the theoretical (red) and experimental (black) FT-IR spectra of (a) BH **I**, (b) BH **II**, and (c) BH **III**.

scaled by Wang et al. as 0.9461.[59] The experimental measurements of ν(C=O) for BH **I**, **II**, and **III** occur at 1663, 1660, and 1667 cm^{-1}, respectively, while the theoretical measurements absorb at 1683, 1688, and 1682 cm^{-1}, respectively, considering the molecule was in the gas phase.

Absorption peaks appear in the experimental $\nu(C_{sp}^2-H)$ aromatic ring for BH **I** at 1606 cm^{-1}, 1580, 1508, and 1457 cm^{-1}; for BH **II** these peaks appear at 1600, 1580, and 1468 cm^{-1}; and for BH **III** they appear at 1606, 1577, and 1486 cm^{-1}, while theoretically, these values appear for BH **I** at 1607 and 1482 cm^{-1}; for BH **II** at 1620, 1575, and 1440 cm^{-1}; and for BH **III** at 1617, 1591, and 1457 cm^{-1}. It is observed that the $\nu(C_{sp}^3-H)$ for BH **I**, **II**, and **III** are in the range of 2965–2853 cm^{-1}, 2972–2845 cm^{-1}, and 2929–2835 cm^{-1}, respectively, while the DFT calculations assigned to the regions of 2957–2876 cm^{-1}, 2935–2859 cm^{-1}, and 2932–2849 cm^{-1}, respectively. Additionally, the experimental measurements of $\nu(C-Cl)$ for BH **II** and **III** are 742 and 799 cm^{-1}, while the theoretical band appears in 746 and 785 cm^{-1}.

Figure 2 shows the BH **I**, **II**, and **III** asymmetric units as an Ortep diagram. With respect to BH **I**, the stereochemistry of the
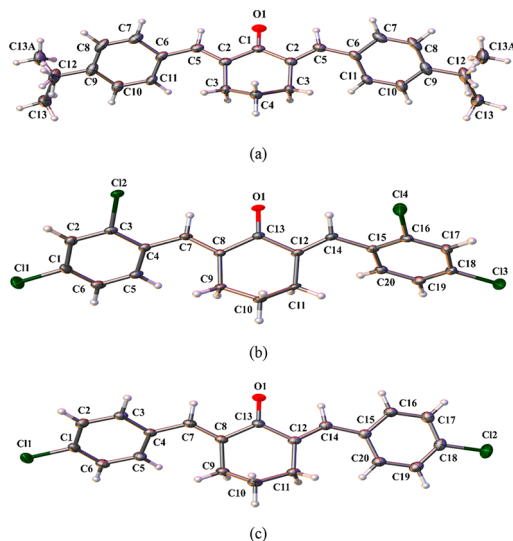

Figure 2. Ortep diagram of ellipsoids at 50% probability level with the atomic numbering scheme for (a) BH **I**, (b) BH **II**, and (c) BH **III**. Hydrogen atoms are in arbitrary radii.

C5═C2 is on an (E)-configuration. This molecule appears in the cyclohexanone as an envelope conformation confirmed by the ring-puckering parameters $Q = 0.5034$ Å and $\phi = 360°$, as described by Cremer and Pople.[60] Additionally, for BH **I**, the dihedral angle C2−C5−C6−C7 has −147.3°, as shown in Table 2. Also, for BH **II** and **III**, the stereochemistry of the C7═C8 and C12═C14 is on an (E,E)-configuration. These molecules appear in the cyclohexanone as a half boat conformation, which is confirmed by the ring-puckering parameters $Q = 0.529$ Å and $\phi = 136.2°$, as well as $Q = 0.5343$ Å and $\phi = 282.02°$ for BH **II** and **III**, respectively. Furthermore, for BH **II** with dichloro-substituted, the dihedral angle C3−C4−C7−C8 and C12−C14−C15−C16 has 145.6° and −142.0°, respectively, as shown in Table 2. Likewise, for BH **III**, the dihedral angle C3−C4−C7−C8 has 149.76°. On the other hand, the dihedral angle C12−C14−C15−C16 between the terminal ring C15−C20 and the cyclohexanone has −173.12°, i.e., almost coplanar, as shown in Table 2.

Relevant experimental and theoretical dihedral angles are given in Table 2. The important crystallographic parameters of BH **I**, **II**, and **III** are shown in Table 3. Detailed intermolecular interactions observed in all crystal structures are given in Table 4.

Table 2. Relevant Experimental and Theoretical Dihedral Angles (deg) for BH I, II, and III

BH	experimental	theoretical
I		
O1−C1−C2−C3	−171.9 (2)	−179.0
C1−C2−C3−C4	−33.4 (2)	−29.8
C1−C2−C5−C6	−176.2 (2)	−179.7
C2−C3−C4−C3	59.9 (3)	59.0
C2−C5−C6−C7	−147.3 (2)	−145.9
C2−C5−C6−C11	36.8 (3)	36.0
C5−C2−C3−C4	144.94 (18)	147.3
C8−C9−C12−C13	−165.1 (3)	−178.1
II		
O1−C13−C8−C9	−173.7 (3)	169.1
O1−C13−C12−C11	−175.5 (3)	−169.1
C13−C8−C9−C10	17.6 (4)	35.4
C12−C11−C10−C9	64.2 (3)	58.7
C13−C8−C7−C4	179.6 (3)	179.2
C13−C12−C14−C15	−176.4 (3)	−179.2
C8−C13−C12−C14	−172.9 (3)	−164.5
C8−C9−C10−C11	−53.4 (4)	−58.7
C12−C14−C15−C16	−142.0 (3)	−134.0
C3−C4−C7−C8	145.6 (3)	134.0
C5−C4−C7−C8	−35.0 (5)	−48.3
C7−C8−C9−C10	−161.2 (3)	−141.0
Cl1−C1−C6−C5	−176.9 (3)	−179.8
Cl2−C3−C2−C1	178.9 (3)	−179.5
Cl3−C18−C17−C16	178.9 (3)	179.9
Cl4−C16−C17−C18	179.6 (3)	179.5
III		
O1−C13−C8−C9	178.3 (1)	178.4
O1−C13−C12−C11	169.0 (1)	−178.4
C13−C8−C9−C10	36.6 (2)	30.1
C12−C11−C10−C9	51.1 (2)	59.0
C13−C8−C7−C4	178.2 (1)	179.9
C13−C12−C14−C15	−179.1 (1)	−179.9
C8−C13−C12−C14	165.6 (1)	−175.7
C8−C9−C10−C11	−63.1 (1)	−59.0
C12−C14−C15−C16	−173.1 (1)	−144.7
C3−C4−C7−C8	149.8 (1)	144.8
C5−C4−C7−C8	−32.4 (2)	−37.0
C7−C8−C9−C10	−140.6 (1)	−147.0
Cl1−C1−C6−C5	−177.6 (1)	−179.5
Cl2−C18−C19−C20	−179.6 (1)	179.5

The BH **I** is crystallized in the orthorhombic system with noncentrosymmetric space group $Cmc2_1$. In this case, being a centrosymmetric molecule and lying on a crystallographic mirror plane, its asymmetric unit comprises only one-half-molecule ($Z' = 0.5$) of the compound. The crystal packing of BH **I** appears in an infinite chain formed by $C_3-H_{3B}\cdots O_1$ interaction along the c axis, which can be described as $C_1^1(5)$[61] (Figure 3a). Further, $C_{13}-H_{13B}\cdots H_{13B}-C_{13}$ dihydrogen contact is possible to observe along the a-axis, also generating an infinite chain (Figure 3b). Figure 3c shows the packing of BH I, formed by dihydrogen contact at the center of the unit cell and the $C_3-H_{3B}\cdots O_1$ interaction lying on a crystallographic mirror plane.

The BH **II** is crystallized in the orthorhombic system with centrosymmetric space group $Pbca$, with one molecule in the asymmetric unit ($Z = 8$). The crystal packing of BH **II** is formed by $C_{10}-H_{10A}\cdots O_1$ and $C_{20}-H_{20}\cdots O_1$ interactions, appearing as bifurcated interaction along the b axis, which can be described as

Table 3. Important Crystallographic Parameters of BH I, II, and III

crystal data	BH I		BH II		BH III	
empirical formula	$C_{24}H_{26}O$		$C_{20}H_{14}OCl_4$		$C_{20}H_{16}OCl_2$	
formula weight/g mol^{-1}	330.45		412.11		343.23	
temperature/K	120(2)		120(2)		120(2)	
radiation type	MoKα		MoKα		MoKα	
crystal system	orthorhombic		orthorhombic		monoclinic	
space group	$Cmc2_1$		$Pbca$		$P2_1/n$	
unit cell dimensions	$a = 20.72(4)$ Å	$\alpha = 90°$	$a = 14.26(2)$ Å	$\alpha = 90°$	$a = 9.82(9)$ Å	$\alpha = 90°$
	$b = 14.80(4)$ Å	$\beta = 90°$	$b = 7.78(13)$ Å	$\beta = 90°$	$b = 16.48(15)$ Å	$\beta = 90°$
	$c = 6.03(12)$ Å	$\gamma = 90°$	$c = 31.37(5)$ Å	$\gamma = 90°$	$c = 10.46(10)$ Å	$\gamma = 90°$
volume/ Å^3	1852.2(7)		3484.7(10)		1630.6(3)	
Z	4		8		4	
density (calculated)/ g cm^{-3}	1.185		1.571		1.398	
$F(000)$	712		1680		712	
reflections collected	14571		61722		30834	
independent reflections	2375 [$R_{(int)} = 0.0356$]		4366 [$R_{(int)} = 0.0856$]		4036 [$R_{(int)} = 0.0223$]	
data/restraints/parameters	2375/1/155		4366/0/238		4036/0/229	
goodness-of-fit on F^2	1.047		1.262		1.077	
final R indexes [$I > 2\sigma(I)$]	$R_1 = 0.0357$, $wR_2 = 0.0868$		$R_1 = 0.0629$, $wR_2 = 0.1289$		$R_1 = 0.0325$, $wR_2 = 0.0785$	
final R indexes [all data]	$R_1 = 0.0448$, $wR_2 = 0.0917$		$R_1 = 0.0793$, $wR_2 = 0.1342$		$R_1 = 0.0379$, $wR_2 = 0.0816$	
extinction coefficient	n/a		n/a		n/a	
largest diff. peak and hole/e Å^{-3}	0.18/−0.19		0.53 and −0.41		0.36 and −0.26	

Table 4. Hydrogen-Bond Geometry (Å, deg) in the Crystal Structure of BH I, II, and III

BH	D−H⋯A	D−H	D⋯A	H⋯A	D−H⋯A	symmetry code
I	C_3−H_{3B}⋯O_1	0.98	3.277	2.55	130.08	$x, y, -1 + z$
	C_{13}−H_{13B}⋯H_{13B}−C_{13}	1.05	2.650	1.65	154.83	$-1 + x, y, z$
II	C_{10}−H_{10A}⋯O_1	0.96	3.506	2.54	177.00	$1/2 - x, 1/2 + y, z$
	C_{20}−H_{20}⋯O_1	0.95	3.225	2.33	157.00	$1/2 - x, -1/2 + y, z$
	C_{17}−H_{17}⋯Cl_3	0.97	3.587	2.74	146.00	$1 - x, -y, 1 - z$
III	C_6−H_6⋯π	0.94	3.623	2.71	159.63	$-1/2 + x, 1.5 - y, -1/2 + z$
	C_{10}−H_{10B}⋯Cl_1	0.97	3.799	2.89	154.87	$-1 + x, y, z$
	C_{18}−Cl_2⋯Cl_1	1.74	5.023	3.30	169.18	$-2 + x, y, -1 + z$

$C_2^1(9)$, as shown in Figure 4a. Further, C_{17}−H_{17}⋯Cl_3 appears as a dimer around the inversion center along the c axis, which can be described as $R_2^2(8)$ (Figure 4b). Figure 4c shows the packing of BH **II**, formed by C_{17}−H_{17}⋯Cl_3 lying at the center of the unit cell and around the inversion centers.

The BH **III** crystallized in the monoclinic system with centrosymmetric space group $P2_1/n$, with one molecule in the asymmetric unit ($Z = 4$). The crystal packing of BH **III**, differently from the other BHs, is formed by C_6−H_6⋯π interaction appearing in a zigzag chain along the a axis (Figure 5a). Further, bifurcated contacts through C_{10}−H_{10B}⋯Cl_1 and C_1−Cl_1⋯Cl_2−C_{18} appears in an infinite chain along the a axis, as shown in Figure 5b. Figure 5c shows the packing of BH **III**, formed by a zigzag chain lying on a crystallographic glide plane. On the other hand, at the center of the unit cell and around the inversion center, no interaction is observed.

In order to interpret the intermolecular interactions, we employed HS d_{norm} analysis. These interactions are verified in d_e and d_i, indicating the distance within the molecule between the external and internal nucleus of the HS, respectively. Additionally, d_e and d_i correspond to acceptor and donor regions, respectively. The HS mapped over d_{norm} (range of −0.511 to 1.470 Å) is shown in Figure 6.

For BH **I**, the red spots correspond to a stronger C_3−H_{3B}⋯O_1 contact (Figure 6a), which is also related to the shorter H⋯H contact (Figure 6b). In the same way, for BH **II**, the red spots

correspond to C_{10}−H_{10A}⋯O_1 and C_{20}−H_{20}⋯O_1 interactions, as shown in Figure 6c. Also, Figure 6d is related to a dimer C_{17}−H_{17}⋯Cl_3 interaction. The shape index HS also is a tool for the identification of hydrophobic interactions like π⋯π. The π⋯π stacking in the BH **II** is identified by the red and blue triangle in the shape index surface, as shown in Figure 6e. The distance between centroids, formed between the center of aromatic rings C1−C6 (Cg1) and C15−C20 (Cg3), is 3.88 Å providing additional stability for the structure. For BH **III**, the red spots correspond to C_6−H_6⋯π and C_{10}−H_{10B}⋯Cl_1 interactions, as shown in Figure 6f,g, respectively. Also, Figure 6h is related to a halogen Cl⋯Cl contact.

The 2D fingerprint plot of BH **I**, **II**, and **III** is shown in Figure 7. From the 2D fingerprint plot, most contact is due to H⋯H interaction, which makes up 68.1% of the HS of BH **I** and is characterized by the thin spike of the fingerprint 2D plot. The contribution of O⋯H/H⋯O interactions of BH **I** represents 5.6% of the HS (Figure 7a). For BH **II**, the contribution of H⋯H and C⋯H/H⋯C contacts represents 23.5% and 15.3% of the HS, respectively. The polar dimer interactions Cl⋯H/H⋯Cl represents 32.7%. Another feature is the existence of C⋯C interaction, which is responsible for 5.1% of HS. The interaction O⋯H/H⋯O is characterized by the small spikes in the bottom of the fingerprint plot, representing 6.0% of the HS, as shown in Figure 7b. For BH **III**, most contact is due to H⋯H interaction which makes up 33.5% of the HS. The contribution of C⋯H/
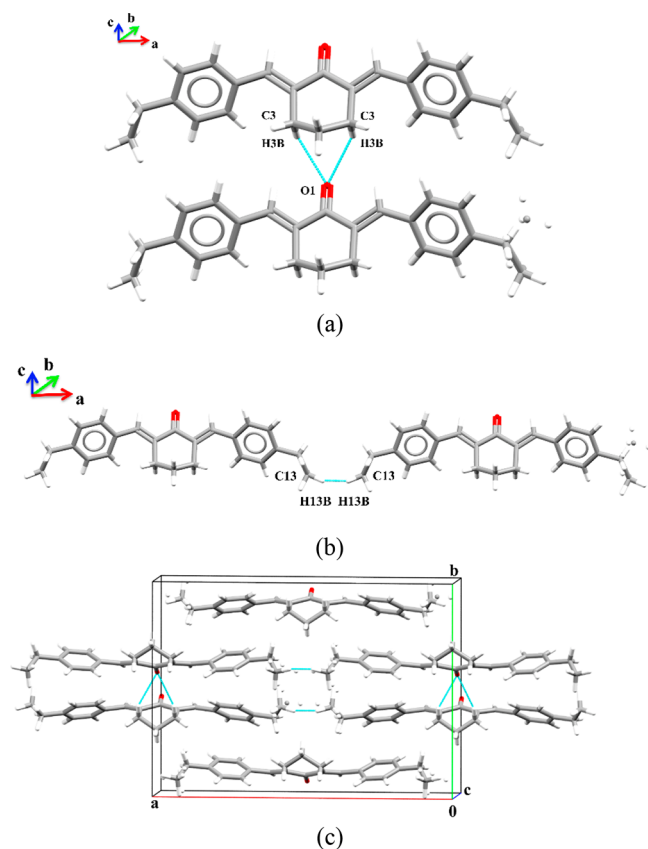
(a)

(b)

(c)

Figure 3. Intermolecular interactions depicting (a) $C_3-H_{3B}\cdots O_1$, (b) $C_{13}-H_{13B}\cdots H_{13B}-C_{13}$ dihydrogen contact, and (c) the crystalline packing of BH **I**.
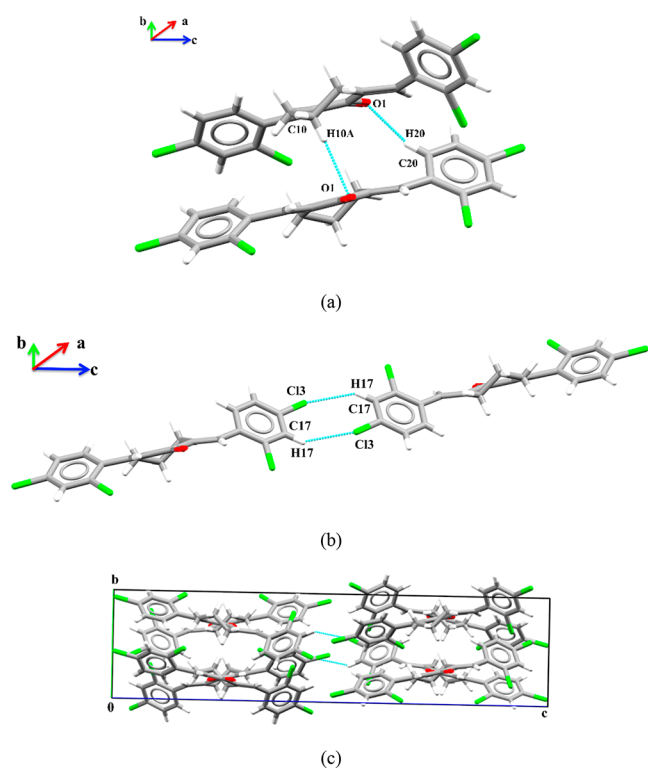

(a)

(b)

(c)

Figure 4. Intermolecular interactions depicting (a) $C_{10}-H_{10A}\cdots O_1$ and $C_{20}-H_{20}\cdots O_1$, (b) $C_{17}-H_{17}\cdots Cl_3$, and (c) the crystalline packing of BH **II**.
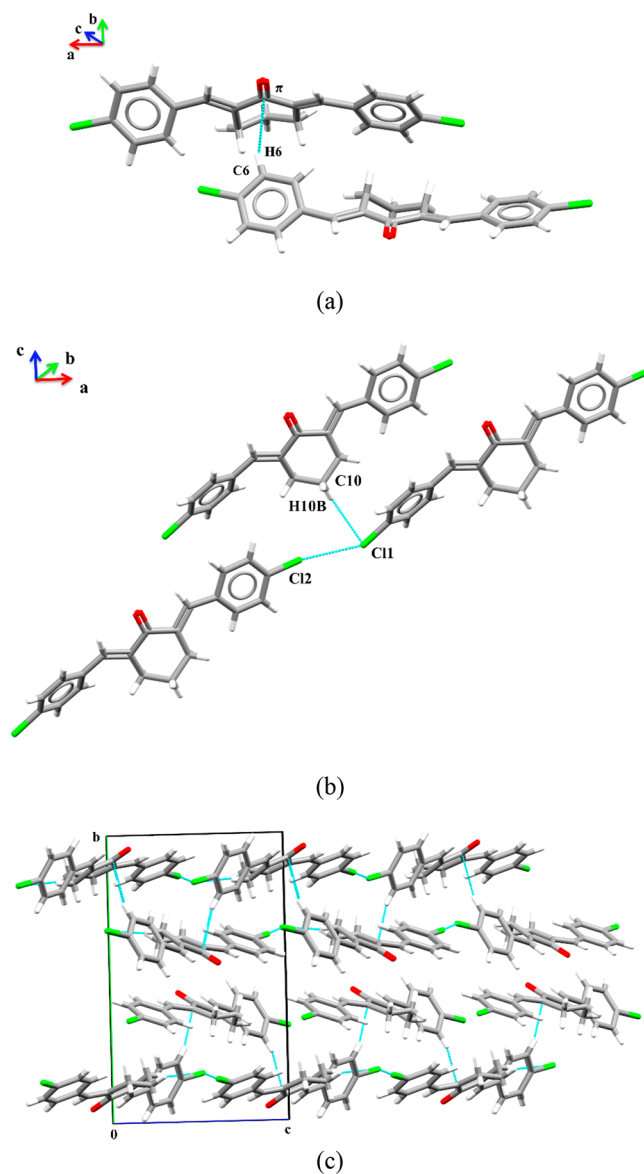

(a)

(b)

(c)

Figure 5. Intermolecular interactions depicting (a) $C_6-H_6\cdots\pi$, (b) $C_{10}-H_{10B}\cdots Cl_1$ and $C_{18}-Cl_2\cdots Cl_1$, and (c) the crystalline packing of BH **III**.

$H\cdots C$ interactions of BH **III** represents 27.4% of the HS. The polar interaction $Cl\cdots H/H\cdots Cl$ represents 22.5%. The contribution of $Cl\cdots Cl$ contacts are characterized by the thin spike at the center of the 2D fingerprint plot (Figure 7c).

The root mean squared (RMS) values predicted by the Mercury program package,[48] comparing calculated and experimental geometries, were 0.0047, 0.0131, and 0.0061 for BH **I**, **II**, and **III**, respectively. The overlay depicts a good correlation between the geometric parameters for all the structures. The difference for BH **I** (Figure 8a), representing about 7.29%, is around C8−C9−C12−C13 with experimental (−165.1°) and theoretical (−178.1°) dihedral angles, as shown in Table 2. The difference for BH **II** (Figure 8b), representing about 7.90%, is around C3−C4−C7−C8 with experimental (145.6°) and theoretical (−134.0°) dihedral angles. Additionally, another difference for BH **II**, representing about 12.5%, is around C7−C8−C9−C10 with experimental (−161.2°) and theoretical (−141.0°) dihedral angles, as shown in Table 2. The difference for BH **III** (Figure 8c), representing about 16.40%, is
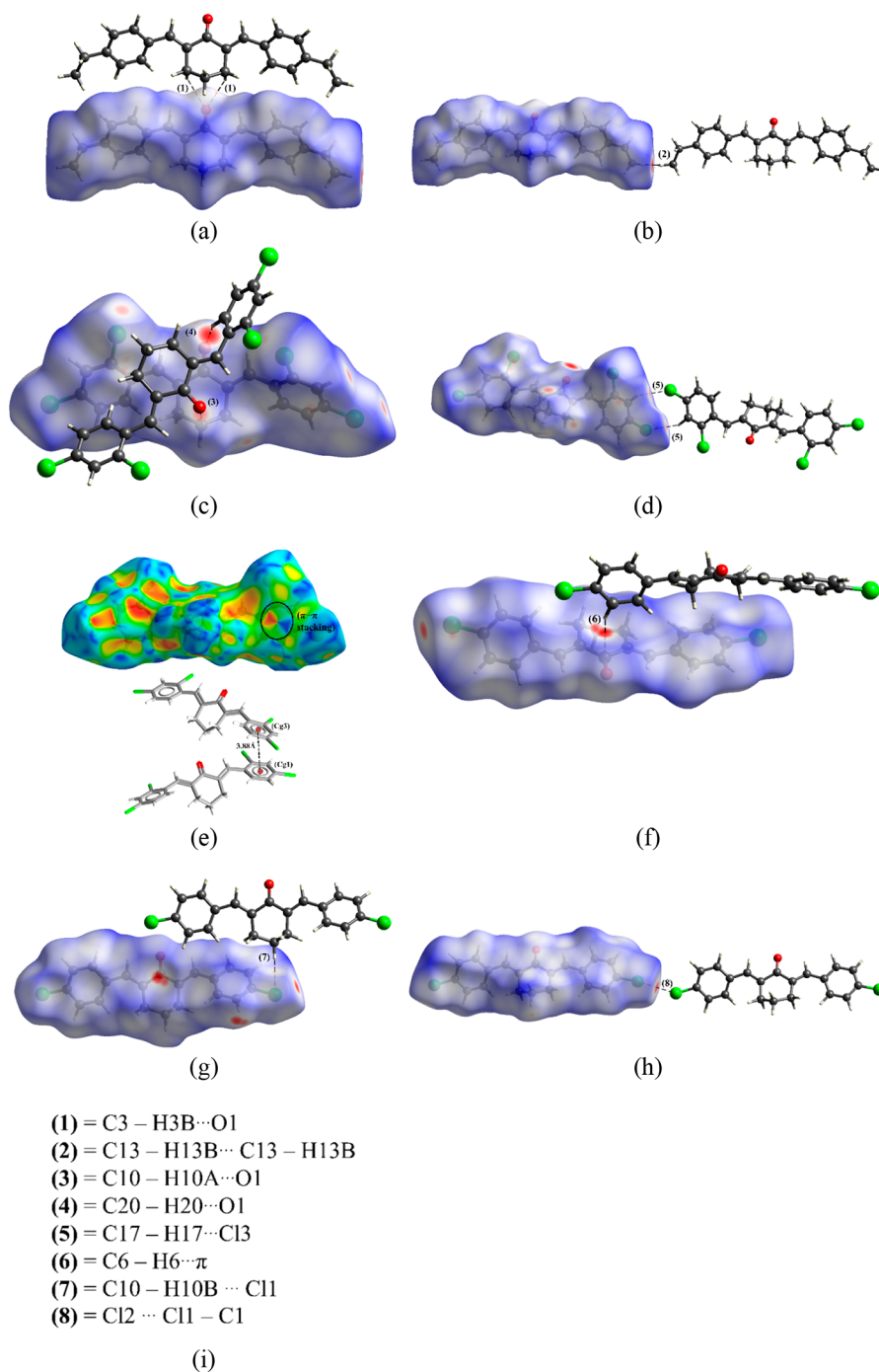
Figure 6. Hirshfeld surfaces indicating (a and b) $C_3-H_{3B}\cdots O_1$ and $C_{13}-H_{13B}\cdots H_{13B}-C_{13}$ intermolecular contacts for BH **I**; (c–e) $C_{10}-H_{10A}\cdots O_1$, $C_{20}-H_{20}\cdots O_1$, $C_{17}-H_{17}\cdots Cl_3$ intermolecular contacts and $\pi\cdots\pi$ stacking for BH **II** and (f–h) $C_6-H_6\cdots\pi$, $C_{10}-H_{10B}\cdots Cl_1$, and $C_{18}-Cl_2\cdots Cl_1$ intermolecular contacts for BH **III** are represented by dotted lines.

around C12−C14−C15−C16 with experimental (−173.1°) and theoretical (−144.7°) dihedral angles, as shown in Table 2.

Supramolecular Modeling Analysis and Energy. The investigation into the chalcones' chemical structure and its properties[62−65] helps us to understand the activity of these molecules as a possible application in fuels.[22] Actually, the world energy matrix has some fuels with advantages over fossil fuels. However, these fuels have stability, oxidation, and energy availability problems, as with ethanol and biodiesel.[28,33] The calorific value test for BH **I**, **II**, and **III** shows values of 7284.0 kcal/kg, 6430.2 kcal/kg, and 7298.7 kcal/kg, respectively (Table 5). In addition, we performed calorific value tests for gasoline (common type C), hydrated ethanol, and *n*-butanol for comparative parameters. Table 5 also presents different calorific values for various types of biodiesel.

The calorific value results reveal that BH **I**, **II**, and **III** have good energy availability, even a little lower than biodiesel (Figure 9). However, BH **I** and **III** (7284.0 and 7298.7 kcal/kg) have a higher calorific value than ethanol (6906.0 kcal/kg), while BH **II** presents a small difference compared to ethanol. Due to the susceptibility and good energy availability of chalcones, they
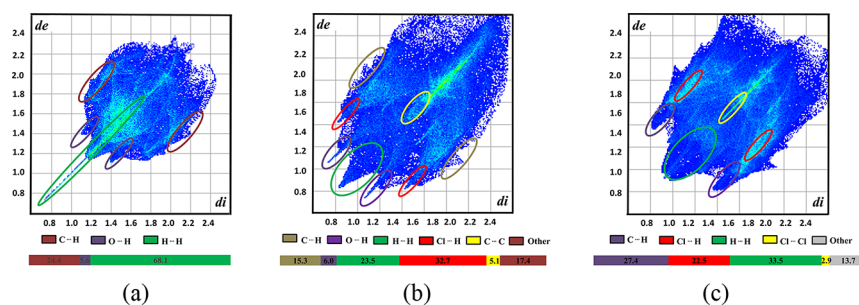
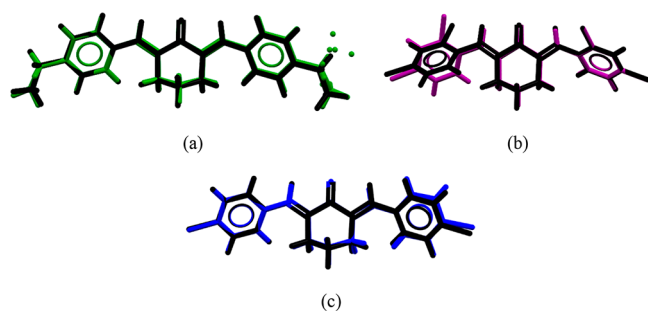**Figure 7.** Fingerprint plot quantifies the contacts for (a) BH **I**, (b) BH **II**, and (c) BH **III**.

Figure 8. Overlapping of theoretical (ωB97XD/6-311++G(d,p)) (black) and X-ray structures for (a) BH **I** (green), (b) BH **II** (purple), and (c) BH **III** (blue) in respect to the aromatic ring.

can be associated with fuels, since the high calorific value in fuels is associated with better performance.

The FMO obtained from Kohn−Sham analysis for BH **I**, **II**, and **III** was carried out at ωB97XD/6-311++G(d,p) level of theory, and they are shown in Figure 10. The FMO analysis of bond-antibonding interactions is a good approximation for ionization (Lewis base) and electron affinity (Lewis acid) energies. The HOMO, the electron donor for BH **I**, **II**, and **III**, is located mainly on the aromatic rings. It is a π-bonding orbital, which is characteristic of the electrophilic region. The HOMO energy for BH **I**, **II**, and **III** is negative (−185.79, −200.34, and −194.86 kcal/mol, respectively). The LUMO for BH **I**, **II**, and **III** is an π-antibonding orbital, and it is spread out through the molecular rings and the carbonyl group. The LUMO energy for BH **I**, **II**, and **III** is −10.69, −20.34, and −19.69 kcal/mol, respectively. These results show that the BH **I**, **II**, and **III** compounds are electrophilic species.

NBO analysis helps us better understand the nature of intermolecular interactions in the solid state. For the reason that one of the aims of this work is to explain the supramolecular arrangement of the BH **I**, **II**, and **III** compounds, the atomic coordinates of non-hydrogen atoms were taken directly from the crystallographic data. However, as the coordinates of the hydrogen atoms were not experimentally determined, it was necessary to optimize them using the wB97XD/6-311++G(d,p) level of theory. The same level of theory was used to obtain the wave function for the NBO analysis. The hyperconjugative interaction energies were estimated from the second-order perturbation formula, as described in eq 4:

$$E(2) = -n_\sigma \frac{\langle\sigma|F|\sigma^2\rangle}{\varepsilon_\sigma^* - \varepsilon_\sigma} = -n_\sigma \frac{F_{ij}^2}{\Delta E'} \tag{4}$$

where $\langle\sigma|F|\sigma\rangle^2$ is the Fock matrix element between the i and j NBO orbitals. ε_σ^* and ε_σ are the energies of σ^* and σ NBO orbitals, respectively, and n_σ stands for the σ donor orbital

Table 5. Calorific Value for BH I, II, III, and Some Fuels[a]

cmpd	calorific value	fuel	calorific value
BH **I**	7284.0	gasoline	9775
BH **II**	6430.2	ethanol	6906
BH **III**	7298.7	butanol	8509

fuel	calorific value	fuel	calorific value
BD-B100 (methyl palm)[66]	8526.7	BD-B100 (rubber seed)[67]	8717.8
BD-B100 (ethyl palm)[66]	9649.4	BD-B100 (sesame)[68]	9649.3
BD-B100 (proplic palm)[66]	8557.9	BD-B10 (soy)[69]	9577.7
BD-B100 (butyl palm)[66]	9941.7	BD-B100 (soy)[69]	8698.7
BD-B100 (pentyl palm)[66]	8776.7	BD-B100 (chicken fat)[70]	9181.2
BD-B100 (maclura pomifera)[71]	9565.7	BD-B100 (olive)[72]	7829.60
BD-B100 (terminalia belerica)[73]	9367.5	BD-B100 (pumpkin)[74]	9095.2
BD-B100 (pongamia pinnata)[75]	8493.3	BD-B100 (rice bran)[76]	10079.2
BD-B100 (rapeseed)[77]	9004.4	BD-B100 (sunflower)[77]	8837.2
BD-B100 (waste vegetable oil)[77]	9052.2	BD-B100 (jatropha)[78]	10564.1
BD-B100 (fish)[79]	9202.9	BD-B100 (neem)[78]	10301.4
BD-B100 (castor bean)[80]	9110.5	BD-B100 (cotton)[78]	10368.3
BD-B100 (argemone mexicano)[81]	9744.9	BD-B30 (watermelon crude oil)[82]	8570.2
BD-B100 (*Cynara cardunculus*)[83]	8885.0	BD-B25 (Pomace - olive)[84]	10399.3
BD-B100 (honge oil)[85]	8622.3	BD-B10 (crambe)[69]	9575.3
BD-B100 (madhuca indica)[86]	8813.4	BD-B100 (crambe)[69]	8760.8
BD-B100 (peanut)[87]	9577.7	BD-B10 (frying oil)[69]	9570.5
BD-B100 (polanga)[88]	9233.7	BD-B100 (frying oil)[69]	8646.2
BD-B100 (roselle)[89]	9434.4	Diesel B0[69,76−78,90]	9646.9−10824.4

[a]All units for calorific power are in kcal/kg. BD: Biodiesel. BD BX, where X refers to the percentage by volume of the biodiesel.

population. NBO analysis provides a method for studying hyperconjugative interaction in a molecular system.[91,92] The higher the $E(2)$ value, the more intensive the interaction between electron donor and acceptor, respectively. Figure 11 shows the calculated NBO orbitals.

For BH **I**, Figure 11a shows the orbital interaction between the lone pair orbital of the O_1 atom and the σ^* antibonding
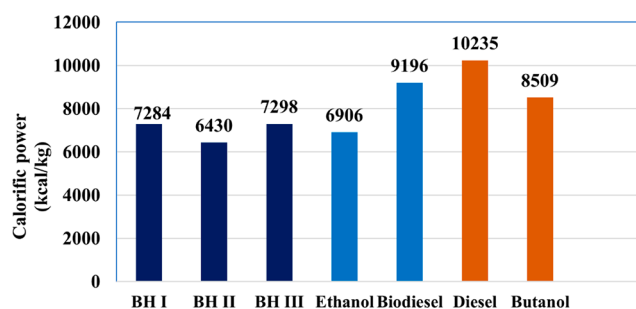
Figure 9. Calorific value for BH **I**, **II**, **III**, and fuels: biodiesel, diesel, hydrated ethanol, and *n*-butanol. The calorific value of biodiesel varies with its composition; therefore, we have a comparative parameter. We performed an average of the values described in Table 5. Average of the values described in Table 5.
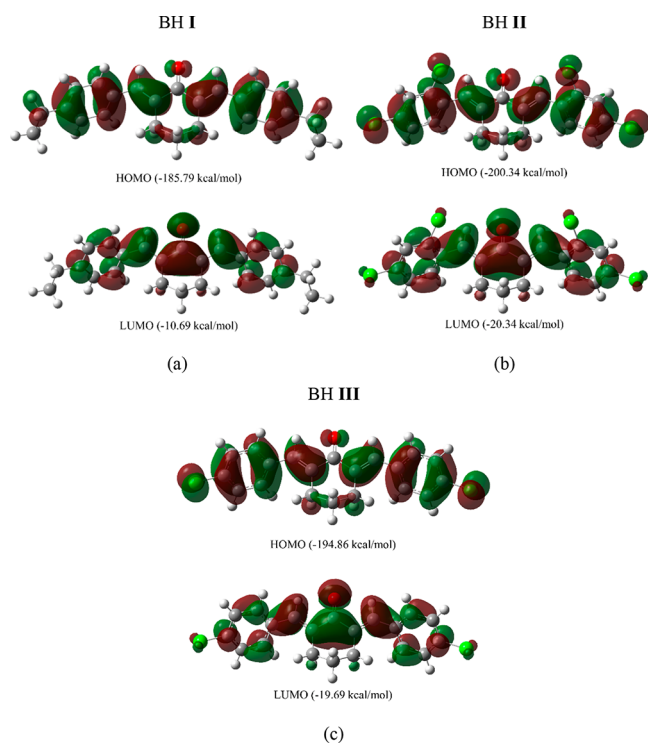

Figure 10. Frontier molecular orbitals derived from Kohn−Sham analysis at ωB97XD/6-311++G(d,p) level of theory with the isovalue of 0.02 atomic units: the HOMO π-bonding orbital and the LUMO π-antibonding orbital for (a) BH **I**, (b) BH **II**, and (c) BH **III**.

orbital of the C_3-H_{3B} with a stabilization energy of 0.38 kcal mol^{-1}. Along with the dihydrogen contacts (Figure 11b), higher stabilization energy is observed (1.00 kcal mol^{-1}). For BH **II**, Figure 11c shows the orbital interaction between the π bonding orbital of the O_1 atom and the σ^* antibonding orbital of the $C_{10}-H_{10A}$ with a stabilization energy of 0.96 kcal mol^{-1}. The orbital interaction between the lone pair orbital of the O_1 atom and the σ^* antibonding orbital of the $C_{20}-H_{20}$ is shown in Figure 11d with a stabilization energy of 1.52 kcal mol^{-1}. Along with the dimer interaction (Figure 11e) between the lone pair orbital of the Cl_3 atom and the σ^* antibonding orbital of the $C_{17}-H_{17}$, it is observed a stabilization energy of 0.53 kcal mol^{-1}.

For BH **III**, Figure 11f shows the orbital interaction between the σ bonding orbital of the C_6-H_6 atom and the π^* antibonding orbital of the O_1-C_{13} with a stabilization energy of 0.49 kcal mol^{-1}. The orbital interaction between the lone pair

orbital of the Cl_1 atom and the σ^* antibonding orbital of the $C_{10}-H_{10B}$ is shown in Figure 11g with a stabilization energy of 0.65 kcal mol^{-1}. Along with the halogen contact (Figure 11h) between the lone pair orbital of the Cl_1 atom and the σ antibonding orbital of the Cl_2, a stabilization energy of 0.63 kcal mol^{-1} is observed.

The MEP is a physicochemical tool that gives information about molecular interactions and helps predict the reactive sites to be targeted in a chemical reaction. The electrostatic potential at a given point $\rho(r)$ in the vicinity of a molecule can be calculated by eq 5:

$$V(r) = \sum_\alpha \frac{Z_\alpha}{|r - R_\alpha|} - \int \frac{\rho(r')}{|r - r'|} \, dr' \tag{5}$$

where $V(r)$ is the potential energy by a positive unit charge at point r; Z_α is the nuclear charge of the atom α located at position R_α, and $\rho(r')$ is the electron density.

The tridimensional MEP representation (Figure 12) for BH **I**, **II**, and **III** shows that the most negative region (red) is located on the oxygen atom of the carbonyl group, with a value of -35.76, -30.93, and -30.12 kcal/mol, respectively. On the other hand, the positive region (blue) is around the cyclohexanone hydrogen atoms, with a value of 12.29, 22.02, and 19.39 kcal/mol, respectively. In conclusion, due to C−H···O interactions in the crystal structures, we can assume an electrophilic attack on this carbonyl group's region.

Also, the supramolecular modeling analysis on the hyperconjugative interaction energies and QTAIM analysis, using theoretical calculations at the ωB97XD/6-311++G(d,p) level of theory, were calculated to prove the existence of intermolecular interactions and to classify their nature. Figure 13 shows that, in quantum mechanic calculations, there are two types of interaction for BH **I**, **II**, and **III** in the solid-state, which we call here as side-to-side and head-to-head dimers. The basis set superposition errors (BSSE) were corrected using the counterpoise procedure as implemented in the g16 program.[57] For BH **I**, Figure 13a shows that the side-to-side dimer interaction energy is -10.60 kcal/mol, showing powerful and attractive energy for dimers. The head-to-head interaction energy (Figure 13b) for BH **I** dimer is 1.19 kcal/mol. This interaction energy is negligible and repulsive for the dimers. Consequently, we can assume that the side-to-side interaction energies are the driving forces for the BH **I** molecular arrangement in the solid-state.

For BH **II**, Figure 13c shows that the side-to-side dimer interaction energy is -19.59 kcal/mol, showing powerful and attractive energy for dimers. The head-to-head interaction energy (Figure 13d) for the BH **II** dimer is -0.53 kcal/mol. Consequently, we can assume that both the side-to-side and head-to-head interaction energies are the driving forces for the BH **II** molecular arrangement in the solid-state.

For BH **III**, Figure 13e shows that the side-to-side dimer $C_6-H_6\cdots\pi$ interaction energy is -10.73 kcal/mol. Further, another side-to-side dimer (i.e., $C_{10}-H_{10B}\cdots Cl_1$) interaction energy is -5.48 kcal/mol, showing powerful and attractive energy for the molecule. As well as BH **I**, the head-to-head $C_{18}-Cl_2\cdots Cl_1$ dimer interaction energy (Figure 13f) for BH **III** is 0.31 kcal/mol. This interaction energy is also negligible and repulsive for the dimers. Consequently, we can assume that the side-to-side interaction energies are the driving forces for the BH **III** molecular arrangement in the solid state.

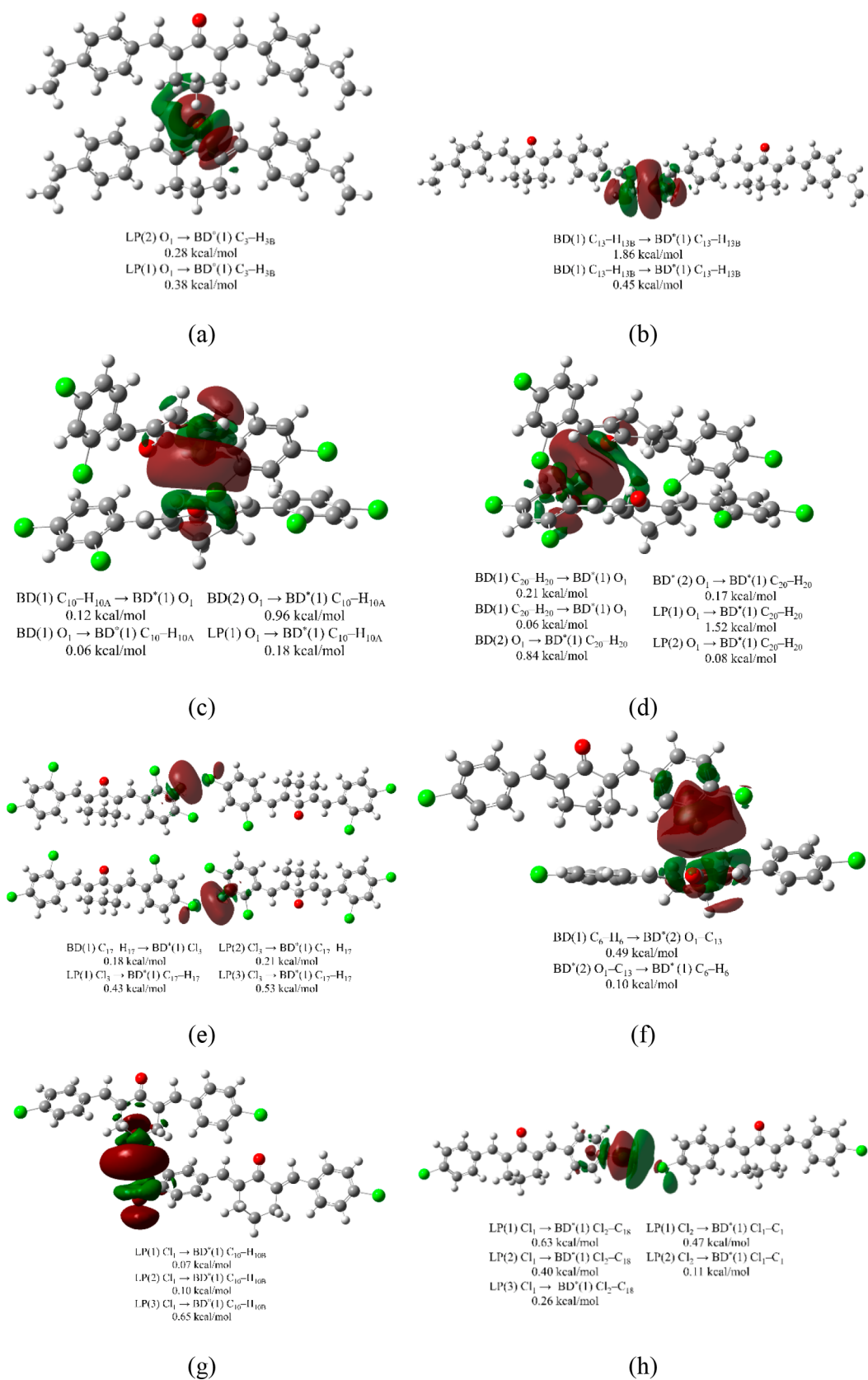The QTAIM analysis was carried out to understand the chemical nature of dimers' interactions.[93,94] The interactions

Figure 11. Intermolecular donor−acceptor natural bond interactions in (a and b) C_3−H_{3B}···O_1 and C_{13}−H_{13B}···H_{13B}−C_{13} for BH **I**; (c−e) C_{10}−H_{10A}···O_1, C_{20}−H_{20}···O_1, and C_{17}−H_{17}···Cl_3 for BH **II**; and (f−h) C_6−H_6···π, C_{10}−H_{10B}···Cl_1, and C_{18}−Cl_2···Cl_1 for BH **III**.

that occur in BH **I** are of type C_3−H_{3B}···O_1 short contact and C_{13}−H_{13B}···H_{13B}−C_{13} dihydrogen contact, as shown by bond

critical point (BCP) analysis (Figure 14). The BCP describes the stationary point between donor and acceptor atoms, confirming

Figure 12. Molecular electrostatic potential surface mapped for (a) BH **I**, (b) BH **II** and (c) BH **III** showing the red-colored region rich in electrons and the blue-colored region, which is electron depleted. The density isovalue of 4.0×10^{-4} electrons/bohr^3 was used to generate the molecular electrostatic potential surfaces.

the existence of hydrogen bonding interaction. The QTAIM's electron density $\rho(r)$ at the BCP of proton-acceptor is 0.032 and 0.050 au for $C_3-H_{3B}\cdots O_1$ and $C_{13}-H_{13B}\cdots H_{13B}-C_{13}$, respectively. The positive Laplacians, 0.040 and 0.28 au for $C_3-H_3\cdots O_1$ and $C_{13}-H_{13B}\cdots H_{13B}-C_{13}$, respectively, are observed for noncovalent hydrogen bonds interactions. The total energy density value $E(r)$ is small and negative for $C_3-H_3\cdots O_1$ and $C_{13}-H_{13B}\cdots H_{13B}-C_{13}$, as shown in Table 6.

The interactions that occur in BH **II** are of type $C_{10}-H_{10A}\cdots O_1$ and $C_{20}-H_{20}\cdots O_1$ short contact and $C_{17}-H_{17}\cdots Cl_3$ dimer interaction, as shown by BCP analysis (Figure 15). The QTAIM's electron density $\rho(r)$ at the BCP of proton-acceptor is 0.058, 0.087, and 0.019 au for $C_{10}-H_{10A}\cdots O_1$, $C_{20}-H_{20}\cdots O_1$, and $C_{17}-H_{17}\cdots Cl_3$, respectively. The positive Laplacians, 0.074, 0.30, and 0.093 au for $C_{10}-H_{10A}\cdots O_1$, $C_{20}-H_{20}\cdots O_1$, and $C_{17}-H_{17}\cdots Cl_3$, respectively, are observed for noncovalent hydrogen bonds interactions. The total energy density value $E(r)$ is small and negative for $C_{10}-H_{10A}\cdots O_1$ and $C_{20}-H_{20}\cdots O_1$, as shown in Table 6. On the other hand, for $C_{17}-H_{17}\cdots Cl_3$, the total energy density value $E(r)$ is small and positive.

The interactions in BH **III** are of type $C_6-H_6\cdots\pi$, $C_{10}-H_{10B}\cdots Cl_1$ short contact and halogen contact $C_{18}-Cl_2\cdots Cl_1$ as shown by BCP analysis (Figure 16). The QTAIM's electron density $\rho(r)$ at the BCP of proton-acceptor is 0.063, 0.053, and 0.025 au for $C_6-H_6\cdots\pi$, $C_{10}-H_{10B}\cdots Cl_1$, and $C_{18}-Cl_2\cdots Cl_1$, respectively. The positive Laplacians, 0.12, 0.19, and 0.014 au for $C_6-H_6\cdots\pi$, $C_{10}-H_{10B}\cdots Cl_1$, and $C_{18}-Cl_2\cdots Cl_1$, respectively, are observed for noncovalent hydrogen bonds interactions. The total energy density value $E(r)$ is small and negative for $C_6-H_6\cdots\pi$ and $C_{18}-Cl_2\cdots Cl_1$, as shown in Table 6. On the other hand, for $C_{10}-H_{10B}\cdots Cl_1$, the total energy density value $E(r)$ is small and positive. We can conclude from the QTAIM analysis that these interactions for all BH **I**, **II**, and **III** dimers can be classified as van der Waals or closed-shell interactions.

Energy availability is directly dependent upon the molecular structure, such as the number of carbons, chemical energy bond interactions, chemical stability, and molecular sites susceptible to the occurrence of reactions. Thus, its thermodynamic properties influence fuel energy efficiency. The difference in the calorific values between BH **I**, **II**, and **III** is related to their supramolecular arrangement formed by chemical energy interactions presented in these compounds. MEP calculation indicates the carbonyl group's region where the burning
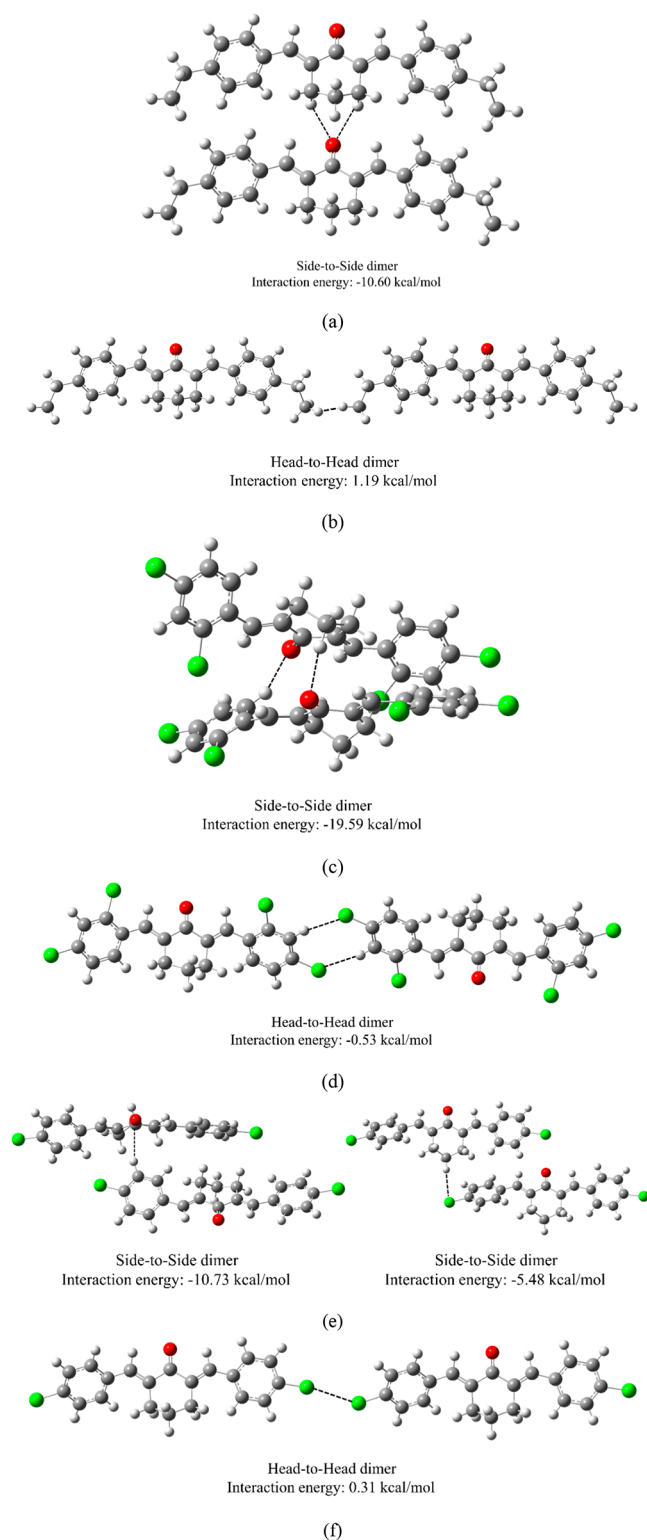

Figure 13. Complexation energies obtained at the ωB97XD/6-311++G(d,p) level of theory: side-to-side and head-to-head dimers, respectively, (a and b) $C_3-H_{3B}\cdots O_1$ and $C_{13}-H_{13B}\cdots H_{13B}-C_{13}$ for BH **I**; (c and d) $C_{10}-H_{10A}\cdots O_1$, $C_{20}-H_{20}\cdots O_1$, and $C_{17}-H_{17}\cdots Cl_3$ for BH **II**; and (e and f) $C_6-H_6\cdots\pi$, $C_{10}-H_{10B}\cdots Cl_1$, and $C_{18}-Cl_2\cdots Cl_1$ for BH **III**.

reactions can occur, which can be involved with higher energy values.[95−97] Additionally, the HOMO and LUMO are related to excitation energies and GAP energy ($E_{GAP} = E_{LUMO} - E_{HOMO}$) in
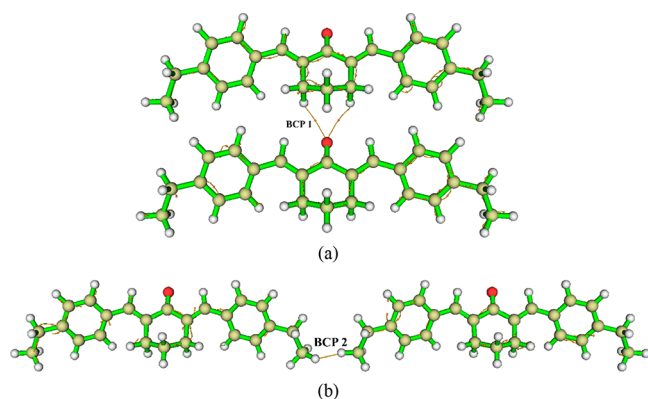
Figure 14. Molecular graph for BH **I**: (a) side-to-side $C_3-H_{3B}\cdots O_1$ interaction and (b) head-to-head $C_{13}-H_{13B}\cdots H_{13B}-C_{13}$ contact, showing the BCP in yellow.
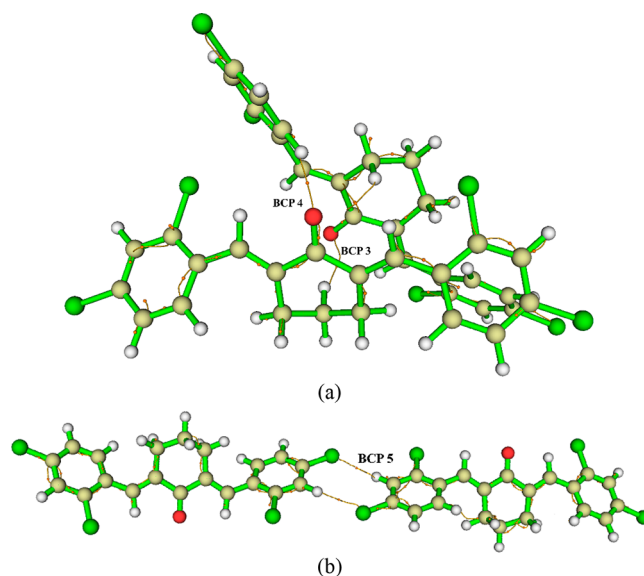

Figure 15. Molecular graph for BH **II**: (a) side-to-side $C_{10}-H_{10A}\cdots O_1$ and $C_{20}-H_{20}\cdots O_1$ short contacts and (b) head-to-head $C_{17}-H_{17}\cdots Cl_3$ dimer interaction, showing the BCP in yellow.

some situations can be an indicator of kinetic stability (large GAP values are associated with kinetic stability).[98−107] For some compounds used to preserve fuels properties, this parameter is described in the literature (toluene derivative [E_{GAP} = 114.1 kcal/mol],[108] butylated hydroxytoluene [E_{GAP} = 130.5 kcal/mol],[109] thiazolidinone [E_{GAP} = 115.1 kcal/mol],[110] ether molecules [E_{GAP} = 96.7 kcal/mol][111]). Note that, according to the GAP values, the molecules analyzed in this work are kinetically more stable (BH **I** 175.1 kcal/mol, BH **II** 180 kcal/mol, BH **III** 175.17 kcal/mol). The structural description of these molecules, theoretical parameters, and experimental analysis of the calorific value provides a good understanding of the structure and its relationship with some properties. This information can support application studies or more specific theoretical analyses.

■ CONCLUSIONS

In this work, three crystal structures of chalcone based on cyclohexanone core have been extensively characterized. All these molecules appear as the dienones in the (E,E)-configuration. For BH **I**, the cyclohexanone appears as an envelope conformation, and for BH **II** and **III**, it appears as a half-boat conformation. The crystal packing for BH **I** was investigated by C−H···H−C dihydrogen contact and non-classical hydrogen bonding C−H···O, which were observed on HS topological analysis (68.1% of H···H interaction and 5.6% of O···H interaction). The crystal packing for BH **II** was

investigated by nonclassical hydrogen bonding C−H···O, C−H···Cl, and π···π stacking, which were observed on HS topological analysis (6.0% of O···H interaction, 32.7% of Cl···H interaction, and 5.1% π···π stacking). The crystal packing for BH **III** was investigated by C−H···π interaction, nonclassical hydrogen bonding C−H···Cl, and halogen Cl···Cl contacts, which were observed on HS topological analysis (27.4% of C···H interaction, 22.5% of Cl···H interaction, and 2.9% Cl···Cl contacts). The calculated and experimental geometries parameters depict a good correlation for all the structures.

The calorific value indicated good energy availability for these compounds, thus being able to support other studies of this application. Theoretical calculations using the counterpoise procedure conclude that the side-to-side interaction energies are the driving forces for the BH **I**, **II**, and **III** molecular arrangements in the solid state. We can conclude from the QTAIM analysis that these interactions for all BH **I**, **II**, and **III** dimers can be classified as van der Waals or closed-shell interactions. Additionally, FMO calculation indicates that the BH **I**, **II**, and **III** compounds are electrophilic species. Also, MEP

Table 6. QTAIM Parameters Describing Contacts and Intermolecular Interactions for BH I, II, and III [Electron Density at BCP ($\rho(r)$), Laplacian ($\bigtriangledown^2\rho(r)$), The Potential Electron Energy Density ($V(r)$), The Kinetic Electron Energy Density ($G(r)$), and The Total Electron Energy Density ($E(r)$). All Values Are Given in Atomic Units (a.u.)]

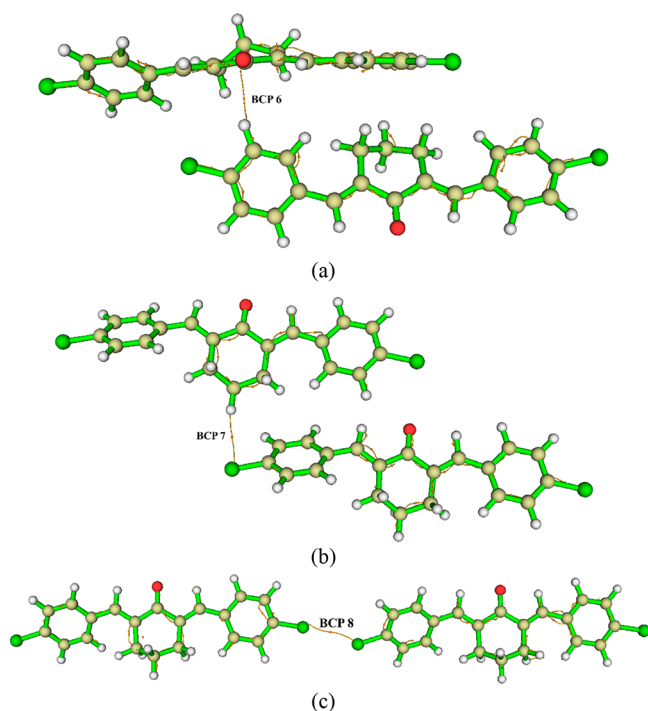| BCP	interaction	$\rho(r)$	$\bigtriangledown^2\rho(r)$	$V(r)$	$G(r)$	$E(r)$	kind of interaction
			BH **I**				
1	$C_3-H_{3B}\cdots O_1$	0.03258	0.04070	−0.01958	0.01488	−0.00470	weak
2	$C_{13}-H_{13B}\cdots H_{13B}-C_{13}$	0.05043	0.28115	−0.10856	0.08942	−0.01913	weak
			BH **II**				
3	$C_{10}-H_{10A}\cdots O_1$	0.05882	0.07459	−0.03009	0.02437	−0.00572	weak
4	$C_{20}-H_{20}\cdots O_1$	0.08763	0.30248	−0.08025	0.07793	−0.00231	weak
5	$C_{17}-H_{17}\cdots Cl_3$	0.01996	0.09355	−0.02006	0.02172	0.00166	weak
			BH **III**				
6	$C_6-H_6\cdots \pi$	0.06380	0.12316	−0.03976	0.03527	−0.0044	weak
7	$C_{10}-H_{10B}\cdots Cl_1$	0.05321	0.19465	0.01753	0.01556	0.03309	weak
8	$C_{18}-Cl_2\cdots Cl_1$	0.02586	0.01479	−0.00782	0.00576	−0.00206	weak

(a)

(b)

(c)

Figure 16. Molecular graph for BH **III**: (a and b) side-to-side $C_6-H_6\cdots\pi$ and $C_{10}-H_{10B}\cdots Cl_1$ short contacts and (c) head-to-head $C_{18}-Cl_2\cdots Cl_1$ contact, showing the BCP in yellow.

calculation indicates the susceptible electrophilic attack on this carbonyl group's region.

ASSOCIATED CONTENT

Ⓢ Supporting Information

The Supporting Information is available free of charge at https://pubs.acs.org/doi/10.1021/acsomega.1c07333.

^{1}H NMR spectra and ^{13}C NMR spectra of compounds BH **I**, **II**, and **III** (PDF)

AUTHOR INFORMATION

Corresponding Authors

Lóide O. Sallum − *Grupo de Química Teórica e Estrutural, Universidade Estadual de Goiás, Anápolis, Goiás 75132-903, Brazil; Laboratório de Novos Materiais, Universidade Evangélica de Goiás, Anápolis, Goiás 75083-515, Brazil;* Email: loide.sallum@gmail.com

Hamilton B. Napolitano − *Grupo de Química Teórica e Estrutural, Universidade Estadual de Goiás, Anápolis, Goiás 75132-903, Brazil; Laboratório de Novos Materiais, Universidade Evangélica de Goiás, Anápolis, Goiás 75083-515, Brazil;* ⓘ orcid.org/0000-0002-6047-9995; Phone: +55 (62) 3328-1192; Email: hbnapolitano@gmail.com

Authors

Vitor S. Duarte − *Grupo de Química Teórica e Estrutural, Universidade Estadual de Goiás, Anápolis, Goiás 75132-903, Brazil; Centro de Pesquisa e Eficiência Energética, CAOA Montadora de Veículos LTDA, Anápolis, Goiás 75184-000, Brazil*

Jean M. F. Custodio − *Grupo de Química Teórica e Estrutural, Universidade Estadual de Goiás, Anápolis, Goiás 75132-903, Brazil;* ⓘ orcid.org/0000-0002-2295-2112

Eduardo C. M. Faria − *Grupo de Química Teórica e Estrutural, Universidade Estadual de Goiás, Anápolis, Goiás 75132-903, Brazil; Centro de Pesquisa e Eficiência Energética, CAOA Montadora de Veículos LTDA, Anápolis, Goiás 75184-000, Brazil*

Aline M. da Silva − *Centro de Pesquisa e Eficiência Energética, CAOA Montadora de Veículos LTDA, Anápolis, Goiás 75184-000, Brazil*

Rosa S. Lima − *Faculdade do Instituto Brasil, Anápolis, Goiás 75133-050, Brazil*

Ademir J. Camargo − *Grupo de Química Teórica e Estrutural, Universidade Estadual de Goiás, Anápolis, Goiás 75132-903, Brazil;* ⓘ orcid.org/0000-0001-9016-222X

Complete contact information is available at:
https://pubs.acs.org/10.1021/acsomega.1c07333

Notes

The authors declare no competing financial interest.

ACKNOWLEDGMENTS

REFERENCES

(1) Vassilev, S. V.; Vassileva, C. G.; Vassilev, V. S. Advantages and Disadvantages of Composition and Properties of Biomass in Comparison with Coal: An Overview. *Fuel* **2015**, *158* (May), 330−350.

(2) Pikula, K.; Zakharenko, A.; Stratidakis, A.; Razgonova, M.; Nosyrev, A.; Mezhuev, Y.; Tsatsakis, A.; Golokhvast, K. The Advances and Limitations in Biodiesel Production: Feedstocks, Oil Extraction Methods, Production, and Environmental Life Cycle Assessment. *Green Chem. Lett. Rev.* **2020**, *13* (4), 275−294.

(3) Lehmann, J. W.; Blair, D. J.; Burke, M. D. Towards the Generalized Iterative Synthesis of Small Molecules. *Nat. Rev. Chem.* **2018**, *2*, 0115 DOI: 10.1038/s41570-018-0115.

(4) Kutulya, L.; Vashchenko, V.; Semenkova, G.; Shkolnikova, N.; Drushlyak, T.; Goodby, J. Chiral Organic Compounds in Liquid Crystal Systems with Induced Helical Structure. *Mol. Cryst. Liq. Cryst.* **2001**, *361*, 125−134.

(5) Pană, A. M.; Păuşescu, I.; Shova, S.; Badea, V.; Tudose, R.; Silion, M.; Costişor, O.; Cseh, L. pH Dependent Structural Interconversion of 2-(2-Hydroxy-Benzylidene)-Cyclohexan-1-One: Crystal Structures and Spectroscopic Investigation. *J. Mol. Struct.* **2017**, *1137*, 9−16.

(6) Yang, J.; Xu, X.; Yang, Y.; Rui, J.; Zhang, Y.; Kuang, H.; Wang, S.; Wu, L. Synthesis, Optical Properties, and Acid-Base Indicating Performance of Novel Ketene Hydroxybenzylidene Nopinone Derivatives. *RSC Adv.* **2016**, *6* (113), 111760−111766.

(7) Borges, I. D.; Danielli, J. A. V.; Silva, V. E. G.; Sallum, L. O.; Queiroz, J. E.; Dias, L. D.; Iermak, I.; Aquino, G. L. B.; Camargo, A. J.; Valverde, C.; Osorio, F. A. P.; Baseia, B.; Napolitano, H. B. Synthesis and Structural Studies on (: E)-3-(2,6-Difluorophenyl)-1-(4-Fluorophenyl)Prop-2-En-1-One: A Promising Nonlinear Optical Material. *RSC Adv.* **2020**, *10* (38), 22542−22555.

(8) Kawamata, J.; Inoue, K.; Inabe, T. Prominent Second-Order Nonlinear Optical Properties of Novel Ketone Derivatives. *Mol. Cryst.*

Liq. Cryst. Sci. Technol. Sect. A-MOLECULAR Cryst. Liq. Cryst. **1996**, *278*, 117−124.

(9) Dimmock, J. R.; Sidhu, K. K.; Quail, J. W.; Jia, Z.; Duffy, M. J.; Reid, R. S.; Kirkpatrick, D. L.; Zhu, L.; Fletcher, S. M. Synthesis and Cytotoxic Evaluation of Some 6-arylidene-2-(−hydroxyamino-α-arylmethyl)Cyclohexanone Oximes and Related Compounds. *J. Pharm. Sci.* **1992**, *81* (11), 1059−1064.

(10) Sallum, L. O.; Siqueira, V. L.; Custodio, J. M. F.; Borges, N. M.; Lima, A. P.; Abreu, D. C.; S. Lacerda, E. d. P.; Lima, R. S.; de Oliveira, A. M.; Camargo, A. J.; Napolitano, H. B. Molecular Modeling of Cytotoxic Activity of a New Terpenoid-like Bischalcone. *New J. Chem.* **2019**, *43* (47), 18451−18460.

(11) Labib, M. B.; Sharkawi, S. M. Z.; El-Daly, M. Design, Synthesis of Novel Isoindoline Hybrids as COX-2 Inhibitors: Anti-Inflammatory, Analgesic Activities and Docking Study. *Bioorg. Chem.* **2018**, *80* (May), 70−80.

(12) Gupta, D.; Jain, D. K. Chalcone Derivatives as Potential Antifungal Agents: Synthesis, and Antifungal Activity. *J. Adv. Pharm. Technol. Res.* **2015**, *6* (3), 114−117.

(13) ElSohly, H. N.; Joshi, A. S.; Nimrod, A. C.; Walker, L. A.; Clark, A. M. Antifungal Chalcones from Maclura Tinctoria. *Planta Med.* **2001**, *67* (1), 87−89.

(14) Dimmock, J. R.; Hamon, N. W.; Hindmarsh, K. W.; Sellar, A. P.; Turner, W. A.; Rank, G. H.; Robertson, A. J. Evaluation of 2-benzylidenecyclohexanones and 2,6-bis(Benzylidene)Cyclohexanones for Antitumor and Cytotoxic Activity and as Inhibitors of Mitochondrial Function in Yeast: Metabolism Studies of (E)-2-benzylidenecyclohexanone. *J. Pharm. Sci.* **1976**, *65* (4), 538−543.

(15) Avupati, V. R.; Yejella, R. P. Chalcomes: A Mini Review. *World J. Pharm. Pharm. Sci.* **2014**, *3* (10), 1713−1742.

(16) Sivakumar, P. M.; Prabhawathi, V.; Doble, M. Antibacterial Activity and QSAR of Chalcones against Biofilm-Producing Bacteria Isolated from Marine Waters. *SAR QSAR Environ. Res.* **2010**, *21* (3), 247−263.

(17) Doan, T. N.; Tran, D. T. Synthesis, Antioxidant and Antimicrobial Activities of a Novel Series of Chalcones, Pyrazolic Chalcones, and Allylic Chalcones. *Pharmacol. & Pharm.* **2011**, *02* (04), 282−288.

(18) Ohkatsu, Y.; Satoh, T. Antioxidant and Photo-Antioxidant Activities of Chalcone Derivatives. *J. Japan Pet. Inst.* **2008**, *51* (5), 298−308.

(19) Cioffi, G.; Escobar, L. M.; Braca, A.; De Tommasi, N. Antioxidant Chalcone Glycosides and Flavanones from Maclura (Chlorophora) Tinctoria. *J. Nat. Prod.* **2003**, *66* (8), 1061−1064.

(20) Bhale, P. S.; Chavan, H. V.; Dongare, S. B.; Shringare, S. N.; Mule, Y. B.; Nagane, S. S.; Bandgar, B. P. Synthesis of Extended Conjugated Indolyl Chalcones as Potent Anti-Breast Cancer, Anti-Inflammatory and Antioxidant Agents. *Bioorg. Med. Chem. Lett.* **2017**, *27* (7), 1502−1507.

(21) Mittelbach, M.; Schober, S. The Influence of Antioxidants on the Oxidation Stability of Biodiesel. *JAOCS, J. Am. Oil Chem. Soc.* **2003**, *80* (8), 817−823.

(22) Trindade, M. ; *Increased Biodiesel Efficiency*; Green Energy and Technology; Springer International Publishing: Cham, Switzerland, 2018;.

(23) Faria, E. C. M.; Duarte, V. S.; De Paula, R. L. G.; Da Silva, A. M.; Fernandes, F. S.; Vaz, W. F.; Oliveira, G. R.; Napolitano, H. B. Comparative Study of Chalcones and Their Potential as Additives for Biofuels. *Energy Fuels* **2021**, *35* (1), 552−560.

(24) Faria, E. C. M.; Duarte, V. S.; Da Silva, A. M.; Fernandes, F. S.; De Paula, R. L. G.; Alonso, C. G.; Oliveira, G. R.; Napolitano, H. B. New Halogen Chalcone with Potential for Application in Biofuels. *Energy Fuels* **2020**, *34* (5), 5958−5968.

(25) Da Silva, C. C.; Pacheco, B. S.; de Freitas, S. C.; Berneira, L. M.; dos Santos, M. A. Z.; Pizzuti, L.; de Pereira, C. M. P. Hydroxychalcones: Synthetic Alternatives to Enhance Oxidative Stability of Biodiesel. *In Green Energy and Technology* **2018**, 81−110.

(26) Lenardao, E. J.; Manke Barcellos, A.; Penteado, F.; Alves, D.; Perin, G. Glycerol as a Solvent in Organic Synthesis. *Rev. Virtual Quim.* **2017**, *9*, 192−237.

(27) Piva, E.; De Oliveira, M.; Rockembach, C. T.; Dias, D.; De Pereira, C. M. P.; Becker, E. M.; Ritter, M.; Gonçalves, P. R.; Dos Santos, M. A. Z.; Martins, R. M.; Pacheco, B. S.; Da Rosa, W. L. de O. *Aplicação de Chalconas Como Reagente Antioxidante Em Biodiesel*. BR Patent 1020130300497 A2, 2013.

(28) Yaakob, Z.; Narayanan, B. N.; Padikkaparambil, S.; Unni K., S.; Akbar P., M. A Review on the Oxidation Stability of Biodiesel. *Renewable and Sustainable Energy Reviews.* **2014**, *35*, 136−153.

(29) Rico, J.; Sauer, I. A Review of Brazilian Biodiesel Experiences. *Renew. Sustain. Energy Rev.* **2015**, *45*, 513−529.

(30) Chandrasekaran, V.; Arthanarisamy, M.; Nachiappan, P.; Dhanakotti, S.; Moorthy, B. The Role of Nano Additives for Biodiesel and Diesel Blended Transportation Fuels. *Transp. Res. Part D* **2016**, *46*, 145−156.

(31) De Oliveira, F. C.; Coelho, S. T. History, Evolution, and Environmental Impact of Biodiesel in Brazil: A Review. *Renew. Sustain. Energy Rev.* **2017**, *75*, 168−179.

(32) Jose, T.; Anand, K. Effects of Biodiesel Composition on Its Long Term Storage Stability. *Fuel* **2016**, *177*, 190−196.

(33) Pullen, J.; Saeed, K. An Overview of Biodiesel Oxidation Stability. *Renew. Sustain. Energy Rev.* **2012**, *16* (8), 5924−5950.

(34) Kumar, N. Oxidative Stability of Biodiesel: Causes, Effects and Prevention. *Fuel* **2017**, *190*, 328−350.

(35) Li, Y.; Gong, J.; Deng, Y.; Yuan, W.; Fu, J.; Zhang, B. Experimental Comparative Study on Combustion, Performance and Emissions Characteristics of Methanol, Ethanol and Butanol in a Spark Ignition Engine. *Appl. Therm. Eng.* **2017**, *115*, 53−63.

(36) Guo, Y.; Wei, H.; Yang, F.; Li, D.; Fang, W.; Lin, R. Study on Volatility and Flash Point of the Pseudo-Binary Mixtures of Sunflowerseed-Based Biodiesel+ethanol. *J. Hazard. Mater.* **2009**, *167* (1−3), 625−629.

(37) Pidol, L.; Lecointe, B.; Jeuland, N. *Ethanol as a Diesel Base Fuel: Managing the Flash Point Issue - Consequences on Engine Behavior*. SAE Technical Paper 2009-01-1807, 2009; DOI: 10.4271/2009-01-1807.

(38) Kwanchareon, P.; Luengnaruemitchai, A.; Jai-In, S. Solubility of a Diesel-Biodiesel-Ethanol Blend, Its Fuel Properties, and Its Emission Characteristics from Diesel Engine. *Fuel* **2007**, *86* (7−8), 1053−1061.

(39) Torres-Jimenez, E.; Jerman, M. S.; Gregorc, A.; Lisec, I.; Dorado, M. P.; Kegl, B. Physical and Chemical Properties of Ethanol-Diesel Fuel Blends. *Fuel* **2011**, *90* (2), 795−802.

(40) Shishkina, S. V.; Solomovich, E. V.; Shishkin, O. V.; Kutulya, L. A.; Vashchenko, V. V. Molecular and Crystal Structure of (1R)-2-Arylidene-p-(4-Menthen)-3-Ones. *J. Struct. Chem.* **2002**, *43* (2), 330−337.

(41) Tolochko, A. S.; Kulishov, V. I.; Kutulya, L. A.; Kuznetsov, V. P.; Vashchenko, V. V. Molecular and Crystal Structures of 1R,4R-Cis-2-(4-Phenylbenzylidene)-n-Menthan-3-One. *Crystallogr. Rep.* **2001**, *46* (2), 214−218.

(42) Kuznetsov, V. P.; Kulishov, V. I.; Kutulya, L. A.; Chepeleva, L. V.; Yarmolenko, S. N. Molecular Structure of Alpha,Beta-Unsaturated Ketones: 2-Benzylidenecyclohexanone and Some of Its Derivatives. *Crystallogr. Rep.* **1999**, *44* (2), 196−203.

(43) Bond, A. D.; Solanko, K. A.; Van De Streek, J.; Neumann, M. A. Experimental Verification of a Subtle Low-Temperature Phase Transition Suggested by DFT-D Energy Minimisation. *CrystEngComm* **2011**, *13* (6), 1768−1771.

(44) Sheldrick, G. *SHELXS: Program for the Solution of Crystal Structures*. University of Gottingen: Gottingen, Germany, 1990.

(45) Sheldrick, G. M. Crystal Structure Refinement with SHELXL. *Acta Crystallogr. Sect. C Struct. Chem.* **2015**, *71*, 3−8.

(46) Dolomanov, O. V.; Bourhis, L. J.; Gildea, R. J.; Howard, J. A. K.; Puschmann, H. OLEX2: A Complete Structure Solution, Refinement and Analysis Program. *J. Appl. Crystallogr.* **2009**, *42* (2), 339−341.

(47) Farrugia, L. J. WinGX and ORTEP for Windows: An Update. *J. Appl. Crystallogr.* **2012**, *45* (4), 849−854.

(48) Macrae, C. F.; Edgington, P. R.; McCabe, P.; Pidcock, E.; Shields, G. P.; Taylor, R.; Towler, M.; Van De Streek, J. Mercury: Visualization and Analysis of Crystal Structures. *J. Appl. Crystallogr.* **2006**, *39* (3), 453−457.

(49) Spek, A. L. Structure Validation in Chemical Crystallography. *Acta Crystallogr. Sect. D Biol. Crystallogr.* **2009**, *65* (2), 148−155.

(50) Spackman, M. A.; Jayatilaka, D. Hirshfeld Surface Analysis. *CrystEngComm* **2009**, *11* (1), 19−32.

(51) McKinnon, J. J.; Spackman, M. A.; Mitchell, A. S. Novel Tools for Visualizing and Exploring Intermolecular Interactions in Molecular Crystals. *Acta Crystallographica Section B: Structural Science.* **2004**, *60*, 627−668.

(52) Spackman, P. R.; Turner, M. J.; McKinnon, J. J.; Wolff, S. K.; Grimwood, D. J.; Jayatilaka, D.; Spackman, M. A. CrystalExplorer: A Program for Hirshfeld Surface Analysis, Visualization and Quantitative Analysis of Molecular Crystals. *J. Appl. Crystallogr.* **2021**, *54*, 1006−1011.

(53) American Society for Testing and Materials. *ASTM D4809-18: Standard Test Method for Heat of Combustion of Liquid Hydrocarbon Fuels by Bomb Calorimeter (Precision Method)*, 2018.

(54) Selvaganapathy, T.; Muthuvelayudham, R.; Jayakumar, M.; Minar Mohamed Lebbai, S.; Murugesan, M.P. Rheological Property Analysis of Pyrolytic Liquid Fuel (PLF) Using ASTM and APHA Standards. *Mater. Today Proc.* **2020**, *26*, 3030−3036.

(55) Frisch, M. J.; Trucks, G. W.; Schlegel, H. B.; Scuseria, G. E.; Robb, M. A.; Cheeseman, J. R.; Scalmani, G.; Barone, V.; Petersson, G. A.; Nakatsuji, H.; Li, X.; Caricato, M.; Marenich, A. V.; Bloino, J.; Janesko, B. G.; Gomperts, R.; Mennucci, B.; Hratchian, H. P.; Ortiz, J. V.; Izmaylov, A. F.; Sonnenberg, J. L.; Williams Ding, F.; Lipparini, F.; Egidi, F.; Goings, J.; Peng, B.; Petrone, A.; Henderson, T.; Ranasinghe, D.; Zakrzewski, V. G.; Gao, J.; Rega, N.; Zheng, G.; Liang, W.; Hada, M.; Ehara, M.; Toyota, K.; Fukuda, R.; Hasegawa, J.; Ishida, M.; Nakajima, T.; Honda, Y.; Kitao, O.; Nakai, H.; Vreven, T.; Throssell, K.; Montgomery, J. A., Jr.; Peralta, J. E.; Ogliaro, F.; Bearpark, M. J.; Heyd, J.J.; Brothers, E. N.; Kudin, K. N.; Staroverov, V. N.; Keith, T. A.; Kobayashi, R.; Normand, J.; Raghavachari, K.; Rendell, A. P.; Burant, J. C.; Iyengar, S. S.; Tomasi, J.; Cossi, M.; Millam, J. M.; Klene, M.; Adamo, C.; Cammi, R.; Ochterski, J. W.; Martin, R. L.; Morokuma, K.; Farkas, O.; Foresman, J. B.; Fox, D. J. *Gaussian 16*, Revision C.01; Gaussian, Inc.: Wallingford, CT, 2016.

(56) Chai, J.-D.; Head-Gordon, M. Long-Range Corrected Hybrid Density Functionals with Damped Atom-Atom Dispersion Corrections. *Phys. Chem. Chem. Phys.* **2008**, *10* (44), 6615−6620.

(57) Boys, S. F.; Bernardi, F. The Calculation of Small Molecular Interactions by the Differences of Separate Total Energies. Some Procedures with Reduced Errors. *Mol. Phys.* **1970**, *19* (4), 553−566.

(58) Lu, T.; Chen, F. Multiwfn: A Multifunctional Wavefunction Analyzer. *J. Comput. Chem.* **2012**, *33* (5), 580−592.

(59) Wang, Y.; Zhang, Y.; Ni, H.; Meng, N.; Ma, K.; Zhao, J.; Zhu, D. Experimental and DFT Studies on the Vibrational and Electronic Spectra of 9-p-Tolyl-9H-Carbazole-3-Carbaldehyde. *Spectrochim. Acta - Part A Mol. Biomol. Spectrosc.* **2015**, *135*, 296−306.

(60) Cremer, D.; Pople, J. A. A General Definition of Ring Puckering Coordinates. *J. Am. Chem. Soc.* **1975**, *97* (6), 1354−1358.

(61) Bernstein, J.; Davis, R. E.; Shimoni, L.; Chang, N.-L. Patterns in Hydrogen Bonding: Functionality and Graph Set Analysis in Crystals. *Angew. Chem., Int. Ed. Engl.* **1995**, *34* (15), 1555−1573.

(62) Zhuang, C.; Zhang, W.; Sheng, C.; Zhang, W.; Xing, C.; Miao, Z. Chalcone: A Privileged Structure in Medicinal Chemistry. *Chem. Rev.* **2017**, *117* (12), 7762−7810.

(63) Patil, C. B.; Mahajan, S. K.; Katti, S. A. Chalcone: A Versatile Molecule. *J. Pharm. Sci. Res.* **2009**, *1* (3), 11−22.

(64) Rozmer, Z.; Perjési, P. Naturally Occurring Chalcones and Their Biological Activities. *Phytochem. Rev.* **2016**, *15* (1), 87−120.

(65) Vasquez-Martinez, Y.; Osorio, M.; San Martin, D.; Carvajal, M.; Vergara, A.; Sanchez, E.; Raimondi, M.; Zacchino, S.; Mascayano, C.; Torrent, C.; Cabezas, F.; Mejias, S.; Montoya, M.; Cortez-San Martin, M. Antimicrobial, Anti-Inflammatory and Antioxidant Activities of Polyoxygenated Chalcones. *J. Braz. Chem. Soc.* **2018**, *30* (2), 286−304.

(66) Cavalcante, M. S.; Conceição, L. R. V.; Bastos, R. R. C.; Costa, A. C. G.; Rocha Filho, G. N.; Zamian, J. R. Poder Calorífico e Aumento Da Cadeia de Ésteres Etílicos. In *52nd Congresso Brasileiro de Quimica*, Recife, Brazil, October 14−18, 2012.

(67) Ramadhas, A.; Jayaraj, S.; Muraleedharan, C. Biodiesel Production from High FFA Rubber Seed Oil. *Fuel* **2005**, *84* (4), 335−340.

(68) Saydut, A.; Duz, M.; Kaya, C.; Kafadar, A.; Hamamci, C. Transesterified Sesame (Sesamum Indicum L.) Seed Oil as a Biodiesel Fuel. *Bioresour. Technol.* **2008**, *99* (14), 6656−6660.

(69) Rigotte, M. R. *Desempenho de Conjunto Motor-Gerador Utilizando Biocombustíveis Sob Cargas Variadas*. Master's Thesis, Universidade Estadual do Oeste do Paraná, Cascavel, Paraná, Brazil, 2014

(70) da Silva, M. J.; da Souza, S. N. M.; Souza, A. A.; Martins, G. I.; Secco, D. Motor Gerador Ciclo Diesel Sob Cinco Proporções de Biodiesel Com Óleo Diesel. *Rev. Bras. Eng. Agrícola e Ambient.* **2012**, *16* (3), 320−326.

(71) Saloua, F.; Saber, C.; Hedi, Z. Methyl Ester of [Maclura Pomifera (Rafin.) Schneider] Seed Oil: Biodiesel Production and Characterization. *Bioresour. Technol.* **2010**, *101* (9), 3091−3096.

(72) Kalligeros, S.; Zannikos, F.; Stournas, S.; Lois, E.; Anastopoulos, G.; Teas, C.; Sakellaropoulos, F. An Investigation of Using Biodiesel/Marine Diesel Blends on the Performance of a Stationary Diesel Engine. *Biomass and Bioenergy* **2003**, *24* (2), 141−149.

(73) Chakraborty, M.; Baruah, D. C.; Konwer, D. Investigation of Terminalia (Terminalia Belerica Robx.) Seed Oil as Prospective Biodiesel Source for North-East India. *Fuel Process. Technol.* **2009**, *90* (12), 1435−1441.

(74) Schinas, P.; Karavalakis, G.; Davaris, C.; Anastopoulos, G.; Karonis, D.; Zannikos, F.; Stournas, S.; Lois, E. Pumpkin (Cucurbita Pepo L.) Seed Oil as an Alternative Feedstock for the Production of Biodiesel in Greece. *Biomass and Bioenergy* **2009**, *33* (1), 44−49.

(75) Sureshkumar, K.; Velraj, R.; Ganesan, R. Performance and Exhaust Emission Characteristics of a CI Engine Fueled with Pongamia Pinnata Methyl Ester (PPME) and Its Blends with Diesel. *Renew. Energy* **2008**, *33* (10), 2294−2302.

(76) Sinha, S.; Agarwal, A. K.; Garg, S. Biodiesel Development from Rice Bran Oil: Transesterification Process Optimization and Fuel Characterization. *Energy Convers. Manag.* **2008**, *49* (5), 1248−1257.

(77) Abuhabaya, A.; Fieldhouse, J. D.; Brown, D. Evaluation of Properties and Use of Waste Vegetable Oil (WVO), Pure Vegetable Oils and Standard Diesel as Used in a Compression Ignition Engine. In *University of Huddersfield, Computing and Engineering Annual Researchers' Conference*, University of Huddersfield, Huddersfield, U.K., December 2010.

(78) Kaisan, M. U.; Abubakar, S.; Ashok, B.; Balasubramanian, D.; Narayan, S.; Grujic, I.; Stojanovic, N. Comparative Analyses of Biodiesel Produced from Jatropha and Neem Seed Oil Using a Gas Chromatography-Mass Spectroscopy Technique. *Biofuels* **2021**, *12* (7), 757−768.

(79) Martins, G. I.; Secco, D.; Rosa, H. A.; Bariccatti, R. A.; Dolci, B. D.; Melegari de Souza, S. N.; Santos, R. F.; Benetoli da Silva, T. R.; Gurgacz, F. Physical and Chemical Properties of Fish Oil Biodiesel Produced in Brazil. *Renew. Sustain. Energy Rev.* **2015**, *42*, 154−157.

(80) Nascimento, M. A. R.; Lora, E. S.; Venturini, O. J.; Maldonado, M. R.; Andrade, R. V.; Correa, P. S. D., Jr.; Haikal Leite, M. A. Utilização Do Biodiesel de Mamona Em Micro-Turbinas a Gás - Testes de Desempenho Térmico e Emissões. In *6th Congresso Internacional sobre Geração Distribuída e Energia no Meio Rural - AGRENER 2006*, Campinas, Brazil, June 6−8, 2006.

(81) Singh, D.; Singh, S. P. Low Cost Production of Ester from Non Edible Oil of Argemone Mexicana. *Biomass and Bioenergy* **2010**, *34* (4), 545−549.

(82) Xavier, J. Performance and Emission Characteristics of Diesel Engine Using Watermelon Seed Oil Methyl Ester. *J. Biol. Sci.* **2020**, *20* (2), 88−93.

(83) Lapuerta, M.; Armas, O.; Ballesteros, R.; Fernandez, J. Diesel Emissions from Biofuels Derived from Spanish Potential Vegetable Oils. *Fuel* **2005**, *84* (6), 773−780.

(84) Çaynak, S.; Gürü, M.; Biçer, A.; Keskin, A.; İçingür, Y. Biodiesel Production from Pomace Oil and Improvement of Its Properties with Synthetic Manganese Additive. *Fuel* **2009**, *88* (3), 534−538.

(85) Banapurmath, N.; Tewari, P.; Hosmath, R. Performance and Emission Characteristics of a DI Compression Ignition Engine Operated on Honge, Jatropha and Sesame Oil Methyl Esters. *Renew. Energy* **2008**, *33* (9), 1982−1988.

(86) Puhan, S.; Vedaraman, N.; Ram, B. V. B.; Sankarnarayanan, G.; Jeychandran, K. Mahua Oil (Madhuca Indica Seed Oil) Methyl Ester as Biodiesel-Preparation and Emission Characterstics. *Biomass and Bioenergy* **2005**, *28* (1), 87−93.

(87) Kaya, C.; Hamamci, C.; Baysal, A.; Akba, O.; Erdogan, S.; Saydut, A. Methyl Ester of Peanut (Arachis Hypogea L.) Seed Oil as a Potential Feedstock for Biodiesel Production. *Renew. Energy* **2009**, *34* (5), 1257−1260.

(88) Sahoo, P. K.; Das, L. M.; Babu, M. K. G.; Naik, S. N. Biodiesel Development from High Acid Value Polanga Seed Oil and Performance Evaluation in a CI Engine. *Fuel* **2007**, *86* (3), 448−454.

(89) Nakpong, P.; Wootthikanokkhan, S. Roselle (Hibiscus Sabdariffa L.) Oil as an Alternative Feedstock for Biodiesel Production in Thailand. *Fuel* **2010**, *89* (8), 1806−1811.

(90) Bari, S.; Saad, I. Improvements of Performance and Emissions of a Diesel-Gen-Set With Biodiesel Having Guide Vanes of Various Angles. In *ASME 2016 International Mechanical Engineering Congress and Exposition*, Phoenix, AZ, November 11−17, 2016;.

(91) Reed, A. E.; Curtiss, L. A.; Weinhold, F. Intermolecular Interactions from a Natural Bond Orbital , Donor-Acceptor Viewpoint. *Chem. Rev.* **1988**, *88*, 899−926.

(92) Weinhold, F.; Landis, C. R. *Valency and Bonding A Natural Bond Orbital Donor-Acceptor Perspective*; Cambridge University Press, 2005.

(93) Matta, C. F., Boyd, R. J., Eds. *The Quantum Theory of Atoms in Molecules: From Solid State to DNA and Drug Design*; Wiley-VCH: Weinheim, Germany, 2007; DOI: 10.1002/9783527610709.

(94) Grabowski, S. J. What Is the Covalency of Hydrogen Bonding? *Chem. Rev.* **2011**, *111* (4), 2597−2625.

(95) Murray, J. S.; Politzer, P. The Electrostatic Potential: An Overview. *Wiley Interdiscip. Rev. Comput. Mol. Sci.* **2011**, *1* (2), 153−163.

(96) Sjoberg, P.; Politzer, P. Use of the Electrostatic Potential at the Molecular Surface. *J. Phys. Chem.* **1990**, *94* (10), 3959−3961.

(97) Brinck, T.; Murray, J. S.; Politzer, P. Molecular Surface Electrostatic Potentials and Local Ionization Energies of Group V-VII Hydrides and Their Anions: Relationships for Aqueous and Gas-Phase Acidities. *Int. J. Quantum Chem.* **1993**, *48* (2), 73−88.

(98) Parr, R. G.; Zhou, Z. Absolute Hardness: Unifying Concept for Identifying Shells and Subshells in Nuclei, Atoms, Molecules, and Metallic Clusters. *Acc. Chem. Res.* **1993**, *26* (5), 256−258.

(99) Liu, X.; Schmalz, T. G.; Klein, D. J. Favorable Structures for Higher Fullerenes. *Chem. Phys. Lett.* **1992**, *188* (5−6), 550−554.

(100) Zhou, Z.; Parr, R. G. Activation Hardness: New Index for Describing the Orientation of Electrophilic Aromatic Substitution. *J. Am. Chem. Soc.* **1990**, *112* (15), 5720−5724.

(101) Maidur, S. R.; Jahagirdar, J. R.; Patil, P. S.; Chia, T. S.; Quah, C. K. Structural Characterizations, Hirshfeld Surface Analyses, and Third-Order Nonlinear Optical Properties of Two Novel Chalcone Derivatives. *Opt. Mater. (Amst).* **2018**, *75*, 580−594.

(102) Gázquez, J. L. Hardness and Softness in Density Functional Theory. In *Chemical Hardness*; Springer-Verlag: Berlin, Heidelberg, Germany, pp 27−43, DOI: 10.1007/BFb0036798.

(103) Irfan, A.; Al-Sehemi, A. G.; Chaudhry, A. R.; Muhammad, S. First Principles Study of the N-Channel Thiophene Based Heterocyclic Chalcones. *Optik (Stuttg).* **2017**, *138*, 349−358.

(104) Omar, S.; Shkir, M.; Ajmal Khan, M.; Ahmad, Z.; AlFaify, S. A Comprehensive Study on Molecular Geometry, Optical, HOMO-LUMO, and Nonlinear Properties of 1,3-Diphenyl-2-Propen-1-Ones Chalcone and Its Derivatives for Optoelectronic Applications: A Computational Approach. *Optik (Stuttg).* **2020**, *204*, 164172.

(105) Yoshida, M.; Aihara, J. Validity of the Weighted HOMO-LUMO Energy Separation as an Index of Kinetic Stability for Fullerenes with up to 120 Carbon Atoms. *Phys. Chem. Chem. Phys.* **1999**, *1* (2), 227−230.

(106) Pearson, R. G. Hard and Soft Acids and Bases—the Evolution of a Chemical Concept. *Coord. Chem. Rev.* **1990**, *100*, 403−425.

(107) Liu, S.; Schauer, C. K. Origin of Molecular Conformational Stability: Perspectives from Molecular Orbital Interactions and Density Functional Reactivity Theory. *J. Chem. Phys.* **2015**, *142* (5), 054107.

(108) Krishna Kumar, V.; Suganya, S.; Mathammal, R. Molecular Structure, Vibrational Spectra, HOMO, LUMO and NMR Studies of 2,3,4,5,6-Penta Bromo Toluene and Bromo Durene Based on Density Functional Calculations. *Spectrochim. Acta Part A Mol. Biomol. Spectrosc.* **2014**, *125*, 201−210.

(109) Chinna Babu, P.; Sundaraganesan, N.; Dereli, Ö.; Türkkan, E. FT-IR, FT-Raman Spectra, Density Functional Computations of the Vibrational Spectra and Molecular Geometry of Butylated Hydroxy Toluene. *Spectrochim. Acta Part A Mol. Biomol. Spectrosc.* **2011**, *79* (3), 562−569.

(110) Mohammed, H.; Attia, S.; Nessim, M.; Shaaban, M.; El-Bassoussi, A. Studies on Some Thiazolidinones as Antioxidants for Local Base Oil. *Egypt. J. Chem.* **2019**, *62* (7), 1219−1234.

(111) Rad, A. S. Al-Doped Graphene as Modified Nanostructure Sensor for Some Ether Molecules: Ab-Initio Study. *Synth. Met.* **2015**, *209*, 419−425.